Research Square

Preprints are preliminary reports that have not undergone peer review.
They should not be considered conclusive, used to inform clinical practice,
or referenced by the media as validated information.

Hydrogeochemical changes and $\delta^{13}C$-DIC signature in a silicate-dominated aquifer during controlled CO_2 release: Insights for monitoring unintended CO_2 leakage at CCS sites

João Pedro T. Zielinski

joao.zielinski@pucrs.br

Pontifical Catholic University of Rio Grande do Sul, PUCRS. Institute of Petroleum and Natural Resources

Fernando Hamerski

Pontifical Catholic University of Rio Grande do Sul, PUCRS. Institute of Petroleum and Natural Resources

Mauren Espinosa Gaspar

Pontifical Catholic University of Rio Grande do Sul, PUCRS. Institute of Petroleum and Natural Resources

William Jeovanini Fucks

Pontifical Catholic University of Rio Grande do Sul, PUCRS. Institute of Petroleum and Natural Resources

Rafael Braga

Pontifical Catholic University of Rio Grande do Sul, PUCRS. Institute of Petroleum and Natural Resources

Gustavo Heck

Pontifical Catholic University of Rio Grande do Sul, PUCRS. Institute of Petroleum and Natural Resources

Victor Hugo J. M. dos Santos

Pontifical Catholic University of Rio Grande do Sul, PUCRS. Institute of Petroleum and Natural Resources

Felipe Dalla Vecchia

Pontifical Catholic University of Rio Grande do Sul, PUCRS. Institute of Petroleum and Natural Resources

Clarissa L. Melo

Pontifical Catholic University of Rio Grande do Sul, PUCRS. Institute of Petroleum and Natural Resources

Pedro Antônio Roehe Reginato

Federal University of Rio Grande do Sul (UFRGS) – Porto Alegre (RS)

Research Article

Keywords: CO_2 leakage, hydrogeochemistry, silicate, monitoring, release experiment

Posted Date: October 28th, 2026

DOI: https://doi.org/10.21203/rs.3.rs-11280438/v1

License: This work is licensed under a Creative Commons Attribution 4.0 International License.
Read Full License

Additional Declarations: No competing interests reported.

Hydrogeochemical changes and δ^{13}C-DIC signature in a silicate-dominated aquifer during controlled CO_2 release: Insights for monitoring unintended CO_2 leakage at CCS sites

João Pedro T. Zielinski [a,b] *, Fernando Hamerski [a], Mauren Espinosa Gaspar [a], William Jeovanini Fucks [a], Rafael Braga [a], Gustavo Heck [a], Victor Hugo J. M. dos Santos [a], Felipe Dalla Vecchia [a], Clarissa L. Melo [a], Pedro Antônio R. Reginato [b]

[a] Pontifical Catholic University of Rio Grande do Sul, PUCRS. Institute of Petroleum and Natural Resources, Avenida Ipiranga, 6681, – TECNOPUC, Building 96J, 90619-900, Porto Alegre, Brazil.

[b] Graduate Program in Water Resources and Environmental Sanitation, Hydraulic Research Institute (IPH), Federal University of Rio Grande do Sul (UFRGS) – Porto Alegre (RS), Brazil.

***Corresponding author (ORCID: 0000-0001-9986-8149)**

Email: jpedro.zielinski@gmail.com; joao.zielinski@pucrs.br

INSTITUTE OF PETROLEUM AND NATURAL RESOURCES (IPR)

6681 Ipiranga Avenue

96J Building

ZIP CODE 90619-900

Porto Alegre, RS - Brazil

Phone: +55 51 3320-3689

Fax: +55 51 3353-8350

Acknowledgments

The authors extend their sincere thanks to the research team at the Institute of Petroleum and Natural Resources (IPR) of the Pontifical Catholic University of Rio Grande do Sul (PUCRS) and to the Graduate Program in Water Resources and Environmental Sanitation (PPGRHSA) of the Hydraulic Research Institute (IPH) at the Federal University of Rio Grande do Sul (UFRGS), where the first author completed his PhD. The authors are also grateful to Rafael Manica (PPGRHSA/UFRGS, Brazil), Fátima Ferreira do Rosário (SMS/ECE/AVP – PETROBRAS S.A.), and Tiago de Vargas (PPGGeo/UFRGS, Brazil) for their valuable feedback during the PhD defense, which contributed to improving the writing of this article and provided additional insights.

Abstract

Changes in groundwater quality because of potential unintended CO_2 leakage at carbon capture and storage (CCS) sites is a critical environmental concern and is often cited as a socioenvironmental barrier to public acceptance. Although CO_2 is not a contaminant, its excessive concentration can induce geochemical reactions with aquifer mineralogy, thereby necessitating the evaluation of potential consequences. Despite recent advances in understanding the geochemical imprint of CO_2-impacted aquifers, few studies have focused on silicate-dominated aquifers rich in altered minerals under near-surface conditions, where precipitation can significantly influence these processes. Thus, this study was designed to evaluate the CO_2–groundwater–mineral interaction within a shallow aluminosilicate porous aquifer derived from granite at the TECNOPUC-Viamão CO_2 experimental site in southern Brazil. The primary objectives were to identify hydrogeochemical alterations and to determine key indicators that signal this process. Gaseous CO_2 was injected at varying rates (5, 10, and 12.5 kg/day) at approximately 3 meters below ground level, and groundwater samples were frequently collected from multilevel monitoring wells within a 5-meter radius. The CO_2 injection spanned 46 days, following a background monitoring campaign, and was succeeded by a two-week postinjection phase, culminating in a final sampling campaign

conducted 137 days after the injection ceased. The hydrochemical evolution of the CO_2–groundwater–mineral interaction was tracked through physicochemical and chemical analyses of major, minor, and trace elements and δ^{13}C-DIC (Dissolved Inorganic Carbon). Despite the influence of atmospheric precipitation on certain parameters, strong correlations ($\rho > 0.70$) were observed between the partial pressure of CO_2 (PCO_2) and variables such as electrical conductivity (EC), pH, ORP, total alkalinity (TA) and δ^{13}C-DIC, as well as Ca, Mg, K, Na, Si, Ba, Sr, Fe, Mn, PO_4^{3-}, and HCO_3^- levels. A clear chronological evolution pattern with increasing injection rates was noted for EC, TA, Ca, Mg, K, Na, Si, Ba, Sr, Fe, and HCO_3^- in the closest wells. Considering the natural seasonal hydrogeochemical variability and the control chart constructed for the hydrostratigraphic unit, the sensitivity to CO_2 interactions, including seasonal effects, indicates that EC, Ca, Mg, Fe, HCO_3^-, Ba, Sr, Mn and δ^{13}C-DIC provided a consistent diagnosis of the interactions. In terms of the risk to water quality, the Fe and Mn concentrations exceeded the limits set by both national and international regulations. This study suggests that this suite of variables enables effective diagnosis and assessment of the impact of unintended CO_2 leaks in CCS projects, provided that they are adequately monitored within a well-established seasonal background.

Keywords: CO_2 leakage, hydrogeochemistry, silicate, monitoring, release experiment

1. Introduction

Carbon capture and storage (CCS), sometimes also referred to as geological carbon storage (GCS), is increasingly recognized as a critical strategy for mitigating climate change by reducing CO_2 emissions to the atmosphere (IPCC 2005; Nelson et al. 2005; Azar et al. 2006; Benson and Cole 2008; Oelkers and Cole 2008). This technology aims to securely store CO_2 in deep underground formations, preventing its release and thus alleviating stress on the Earth's climatic system. However, the geological complexity of storage sites, which may include faults, fractures, and small cracks in caprocks, presents significant challenges. If CO_2 leakage occurs at a CCS site, the solubility of CO_2 in water can lead to the formation of carbonic acid, resulting in localized acidification of shallow groundwater above the storage site (Assayag et al. 2009). This acidification can have profound effects on groundwater quality by promoting the dissolution of aquifer rocks, thereby increasing the concentrations of cations and potential trace metals, including Ca, Mg, Fe, Mn, Ba and Sr (Benson et al. 2002; Lawter et al. 2016; Wang et al. 2016; Qafoku et al. 2017; Xiao et al. 2017).

Further geochemical reactions, such as ion exchange, surface complexation, and the precipitation of secondary minerals, can also alter groundwater chemistry because of CO_2 leakage (Zheng et al. 2012; Cahill and Jakobsen 2015). The potential migration of CO_2- and CO_2-rich fluids into freshwater aquifers can degrade drinkable groundwater, highlighting the importance of comprehensive environmental monitoring systems. Hydrochemical and isotopic analyses have proven essential for detecting CO_2 leakage and assessing its impact on groundwater quality (Humez et al., 2014a; Kharaka et al., 2010; Newell et al., 2014; Schulz et al., 2012). Understanding the pattern and degree of geochemical changes at specific sites is crucial not only for detecting leakage but also for managing undesirable effects, such as the mobilization of toxic elements and the decrease in the aquifer's buffering capacity (Lions et al. 2014). Addressing these risks through rigorous monitoring, including the use of hydrochemical indicators and monitoring tools, is vital for the safe, long-term, and effective storage of CO_2. These measures are necessary to mitigate public concern and ensure the successful demonstration and commercialization of GCS technology (Cuéllar-Franca and Azapagic 2015).

Consequently, implementing effective monitoring, measurement, and verification (MMV) strategies is crucial for ensuring the safe storage of CO_2 in deep geological formations and for gaining public acceptance of these technologies. A key and cost-effective approach to better understanding the interactions between CO_2, groundwater, and minerals is the controlled injection of CO_2 into the subsurface. This method allows researchers to track hydrogeochemical changes within the aquifer, providing valuable insights into the processes governing CO_2 behavior and its potential impacts on groundwater quality.

Several studies employing this approach have been published over the past 15 years (Lee et al. 2016; Zielinski et al. 2023), documenting changes in groundwater chemistry resulting from interactions with CO_2 and aquifer mineralogy, including carbonate, mixed-mineralogy, and silicate-dominated systems. These studies have been conducted under a range of hydraulic conductivities: low ($\leq$ 2 m/day), intermediate (2–20 m/day), and high ($\geq$ 20 m/day). Additionally, the total mass and rate of leaked CO_2, the duration of injection, and the timing of preinjection and postinjection monitoring campaigns were varied. This variation in parameters allows the simulation of a broader range of hydrogeochemical responses that might occur in different leakage scenarios. While still limited in number, these studies have collectively advanced the understanding of the potential impacts of CO_2 leakage on groundwater quality. However, only a limited number of studies have assessed the effects of silicate-dominated aquifers rich in altered minerals, such as clays and oxides (Do et al., 2022), under shallow conditions (Kharaka et al., 2010). In this context, groundwater systems exhibit weaker carbonate buffering capacity, distinct ion exchange and adsorption behaviors, and different trace element mobilities. Moreover, shallow aquifers are generally more responsive to recharge and mixing processes than deeper systems are, which further affects the geochemical signature of CO_2-impacted groundwater.

Furthermore, to the best of the authors' knowledge, no studies have yet included experiments that combine these characteristics within a humid subtropical climate, which are characterized by a mean annual precipitation of approximately 1,500 mm, relatively uniform rainfall distribution throughout the year, and pronounced seasonal temperature variations, with summer temperatures (December–March) often exceeding 32°C and winter temperatures (June–September) occasionally falling below 5°C. This climatic regime directly affects infiltration rates, thereby influencing groundwater mixing and dilution processes, the prevailing redox conditions, and the generation of soil-derived CO_2. Thus, the primary objective of this study was to design and implement a controlled CO_2(g) leakage experiment within a shallow groundwater aquifer located in a silicate formation resulting from granite alteration at TECNOPUC/Viamão in Rio Grande do Sul, southern Brazil (Zielinski et al. 2024). Experiments were conducted under varying CO_2 leakage rates and precipitation events to explore the hydrogeochemical responses and interactions within this geological setting. Spatiotemporal changes in groundwater physicochemical properties (pH, EC, ORP, DO, and alkalinity), major dissolved constituents (HCO_3^-, Ca, Mg, Na, K, Si, SO_4^{2-}, Cl^-, NO_3^-, and PO_4^{3-}), trace elements (Fe, Mn, Sr, and Ba), and the isotopic composition of dissolved inorganic carbon (δ^{13}C-DIC) were monitored using samples collected from wells positioned both upgradient and downgradient of groundwater flow. Multivariate statistical techniques, such as principal component analysis (PCA) and correlation analysis (CA), were used to identify CO_2-impacted groups and track changes in hydrochemical variables relative to the partial pressure of CO_2 (PCO_2). Additionally, anomalous hydrochemical parameters (based on control-chart limits) were compared with long-term (>3 years) natural background variations to assess their sensitivity to CO_2 injection. Parameters exceeding contaminant levels were evaluated against regulatory guidelines and existing studies to assess potential environmental risks to groundwater quality.

2. Materials and methods

The TECNOPUC-Viamão controlled-release experimental site (U^{TM} Zone 22, Southern Hemisphere, 494315 mE & 6671940 mN), Rio Grande do Sul state, southern Brazil, is a practical research field facility of the Pontifical Catholic University of Rio Grande do Sul (PUCRS), which comprises a granite-derived weathered soil profile located 20 km away from the state's capital Porto Alegre (Melo et al. 2017; Iglesias et al. 2019; Zielinski et al., 2024). Established in 2015 and covering an area of ca. 6,000 m^2, the field facility—maintained and operated by the Institute of Petroleum and Natural Resources (IPR)—has four sets of three multilevel wells each (Figure 1), totaling twelve groundwater monitoring wells (MW) that were designed for water sampling campaigns. Wells are named by the prefix M and a suffix according to their installed depth (Table 1).

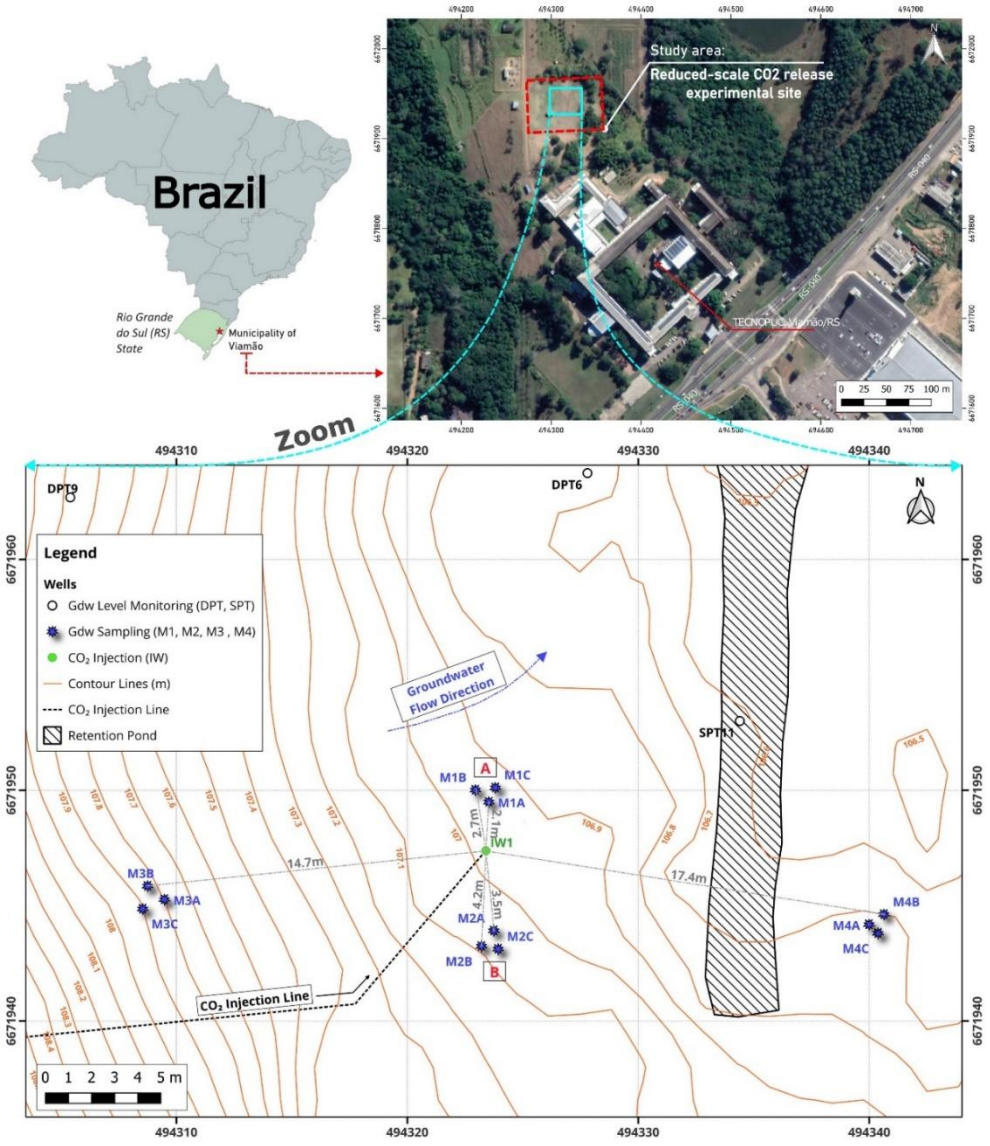


Fig 1 Location map of the small-scale TECNOPUC-Viamão experimental CO_2 release site and the installed infrastructure. Multilevel sampling wells are shown in blue, with the gray dashed line representing the linear distance between the injection well (IW1) and each sampling well. Groundwater generally flows toward the northeast (NE). Letters A and B (in red) illustrate the transect between M1 and M2, as detailed in Figure 2

Table 1. Installed water sampling wells and their corresponding screening intervals. The sampling depth indicates the distance from the surface to the point of water extraction, where samples were collected during each sampling campaign.

Well	Installed depth (m)	Screened Interval (m)	Sampling depth (m)
M1A	1	0.5–1	0.75
M2B	2.5	1–2.5	2
M2C	3.5	2.5–3.5	NS
M2A	1	0.5–1	0.75
M2B	2.5	1–2.5	2
M2C	3.5	2.5–3.5	NS
M3A	1	0.5–1	NS
M3B	2.5	1–2.5	2
M3C	3.5	2.5–3.5	NS
M4A	1	0.5–1	NS
M4B	2.5	1–2.5	2
M4C	3.5	2.5–3.5	NS

Note: depths are referenced by surface (ground) level, not by the tip of the wellhead, and therefore represent depth below ground level (bgl); NS means not sampled.

In this study, wells M1A, M1B, M2B, M3B and M4B were selected and used for hydrochemical and isotopic evaluation of the CO_2–groundwater–mineral interaction, as they were either near the CO_2 injection well or upstream/downstream of the groundwater flow direction. Wells M1C, M2C, M3C, and M4C were not sampled during the study, as they either yielded insufficient water volumes for laboratory analyses or were dry at the time of sampling. Although well M2A was sampled only twice, its omission from further statistical analysis is not expected to influence the results because its hydrochemical composition closely resembles that of well M2B. On the basis of the described mineralogical composition, vertical soil texture distribution, and characterized hydraulic conductivity, the geological strata were classified into four hydrostratigraphic units (from top to bottom): i) organic soil (So); ii) silt (St); iii) sandy clay (Aa); and iv) altered granite (Ga). CO_2 injection was conducted within the sandy clay (Aa) unit in its gaseous state. Given the natural groundwater flow and the lower density of CO_2 (g), groundwater samples were collected from levels A and B (Figure 2).

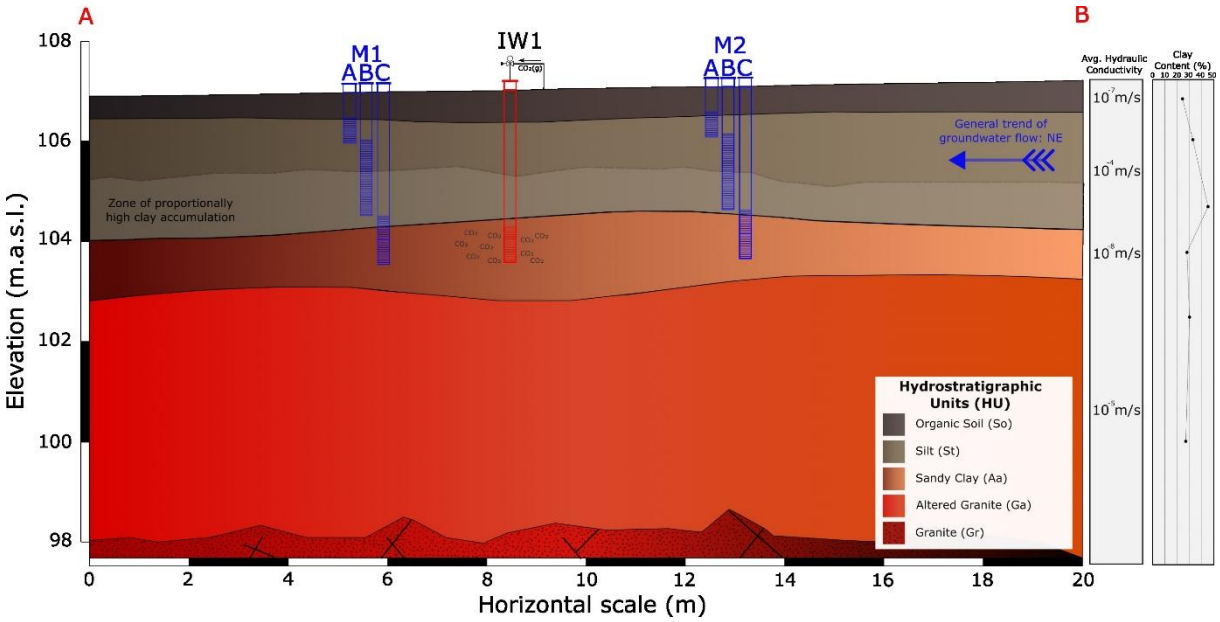


Fig 2 Hydrostratigraphic units and construction characteristics of the monitoring wells (M1 and M2) and injection well (IW1). Letters A and B correspond to the section referenced in the location map of Figure 1. Wells M1A/B and M2A/B are screened almost entirely within the St unit, which is also intercepted by wells M3A/B and M4A/B

The wells sampled within the HU St unit are primarily composed of feldspars, micas, quartz (SiO_2), amphiboles, and opaque minerals, with K-feldspar being the most prevalent. Orthoclase ($KAlSi_3O_8$) is more abundant than microcline ($KAlSi_3O_8$) and presents a range of colors, contributing to variations in the coloration of the sandy fraction. Plagioclase, represented mainly by albite ($NaAlSi_3O_8$) and oligoclase ($(Na,Ca)(Si,Al)_4O_8$), is also present but in lower proportions than K-feldspar. Muscovite ($KAl_2(AlSi_3O_{10})(OH)_2$) is the dominant mica, with subordinate occurrences of biotite ($K(Mg,Fe)_3AlSi_3O_{10}(F,OH)_2$). Kaolinite ($Al_2Si_2O_5(OH)_4$) is the most abundant clay mineral, whereas illite ($K_{0.65}Al_{2.0}(Si_{3.35}Al_{0.65})O_{10}(OH)_2$) and interstratified clay minerals constitute a secondary fraction, along with trace amounts of goethite (FeO(OH)) and lepidocrocite (γ-FeO(OH)).

Slug tests conducted in wells screened at intervals A and B yielded relatively consistent hydraulic conductivity values ranging from 10^{-4} to 10^{-5} m/s for the HU St unit. Although effective porosity was not determined at the site and the hydraulic gradient lies within the uncertainty associated with water table fluctuation measurements (centimeter scale), groundwater displacement is expected to exceed the distance between IW1 and wells M1 and M2. This interpretation is based on typical porosity values for silt-sized unconsolidated deposits (35–50%;(Freeze and Cherry 1979) and hydraulic gradients in the range of 0.003 to 0.01. For a more detailed discussion of the geological and hydrogeological characteristics and the geoelectrical model of the study area, see Zielinski et al. (2024).

2.1. Design and execution of the controlled-release CO_2 experiment

The experiment was planned to have three main phases: i) a background, which consisted of three sampling campaigns (SB); ii) an injection phase composed of sixteen sampling campaigns (SI); and iii) a postinjection phase, which consisted of five sampling campaigns (SP). The first one-week immediate background campaign, which defined the groundwater baseline composition and natural hydrochemical range, included SB1, SB2 and SB3, which were carried out from January 8 to January 12. The injection phase took place between January 15 and

March 1 (46 days) and included SI4 to SI20. The concentrated postinjection phase occurred between March 5 and March 15 (SP21 to SP24), followed by a final sampling campaign 124 days after March 15 (SP25) to check for groundwater background attainment.

CO_2(g) was released to the subsurface at IW1 between 2.7 and 3 m deep through a vertical well, which is at least 0.7 m below the first sampling point of the nearest MW (M1B and M2B). In contrast to the studies of Do et al. (2022) and Cahill et al. (2014), which employed inclined injection wells, a vertical injection well was adopted in this study because the specialized equipment and technical capabilities required for directional drilling were not available during the field campaign. Therefore, the vertical configuration was the most technically feasible option under the site conditions. Notably, the shallow depth of the experimental site was intentionally selected to enable the use of other near-surface CO_2 monitoring techniques (e.g., soil CO_2 flux chambers). Under these conditions, upward CO_2 migration was likely enhanced, and an important fraction of the injected CO_2 may have reached the ground surface, representing an inherent limitation of the experimental setup.

The injection system consists of an injection plant actionable by an electronic device (backed up by a manual control system) that is directly connected to CO_2 cylinders through a manifold. A mass flow controller (MFC) regulates the injection rate according to a predefined setpoint. After passing through the release valve, the CO_2 enters the tracer chamber before it reaches the injection well, which is equipped with a gas sampling port at the wellhead used to collect injected CO_2 for isotopic signature analysis (Figure 3). A tracer chamber was installed to track CO_2 gaseous-phase behavior using perfluoromethylcyclopentane (PMCP) as a tracer in the soil gas phase. However, as these results fall outside the scope of the present study, they are not reported here.

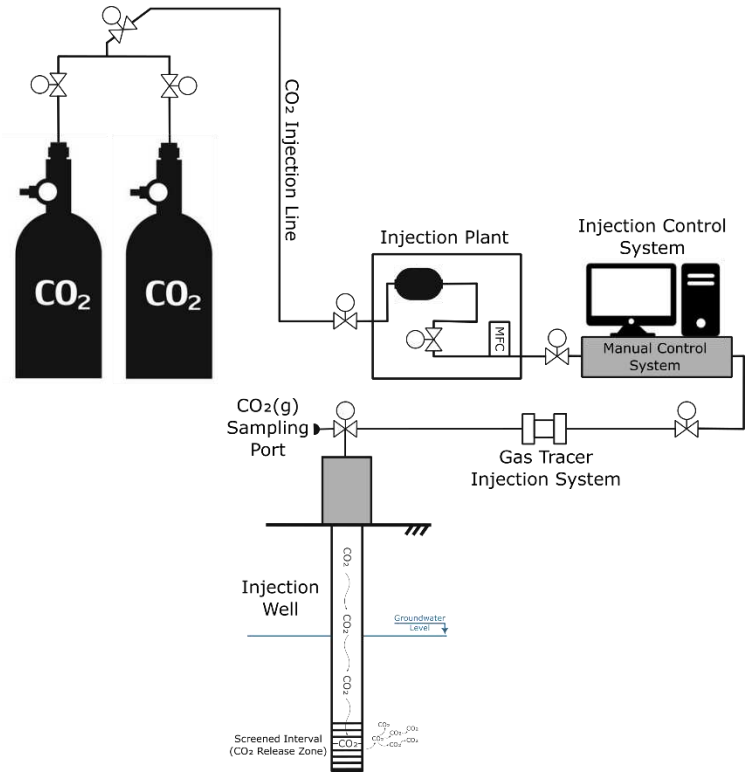


Fig 3 Simplified schematic sketch of the CO_2 injection system and its associated components from the cylinder to the injection well

The controlled release (injection) of CO_2 started on January 15, with a nominal injection rate of 5 kg of CO_2/day, which was increased to 10 kg of CO_2/day on January 29 because of the subtle changes in physicochemical parameters (no further decrease in pH and a slight increase in EC) observed onsite during the sampling procedure and to compensate for possible dilution caused by rainwater recharge events that occurred during that period. On February 15, the release rate was again increased to 12.5 kg of CO_2/day for the last two weeks of the experiment to increase the CO_2–groundwater–mineral interaction. Injection stopped on March 2 at approximately midnight. On the basis of the calculations performed, around 430 (± 5%) kg of CO_2 was released throughout the injection phase. The progressive increases in the injection rate were intended to maintain the detectability of CO_2-induced hydrogeochemical responses under the transient hydrological conditions characteristic of this shallow system, which was subject to uncontrolled external influences, primarily variations in rainfall recharge and their associated effects. Precipitation data were collected using an automated weather station (Plugstation® WS22, Plugfield) near the field office and approximately 50–60 m from the monitoring wells, ensuring high spatial representativeness of precipitation measurements across the experimental site.

2.2. Sampling procedure and chemical analysis

Groundwater sampling operations were conducted periodically to track hydrochemical and carbon isotopic variations as the CO_2 release progressed. A total of 25 sampling campaigns were conducted (Table 2), yielding a total of 116 samples: a) M1A (n=17 samples); b) M1B (n=25 samples); c) M2A (n=2 samples); d) M2B (n=25 samples); e) M3B (n=25 samples); and f) M4B (n=22 samples). Sampling was conducted according to the low-flow method as specified in the NBR 15847 standard (ABNT 2010), which is based on ASTM's D6452 (AS^{TM} 2018) and D4448 (AS^{TM} 2019) guidelines. A Millipore® Easy-Load peristaltic pump integrated into a closed-system flow cell equipped with a QED® MP-20 multiparameter probe provided field measurements of groundwater temperature, hydrogen potential (pH), electrical conductivity (EC), redox potential (ORP) and dissolved oxygen (DO). Total alkalinity was measured in the laboratory by titration with a 0.1 N H_2SO_4 solution.

Table 2. Sampling campaigns were conducted during the background (BG), injection, and postinjection (PI) periods, indicating the number of wells sampled and the relative timing of each campaign with respect to the start date of CO_2 injection.

Sampling Campaign	***Campaign Phase***	***Days before/since injection***	***Date***	***N° of sampled wells***
SB1	*BG*	*-7*	*Jan 8, 2024*	*3*
SB2		*-5*	*Jan10, 2024*	*4*
SB3		*-3*	*Jan 12, 2024*	*5*
SI 4	*Injection*	*0**	*Jan 15, 2024*	*4*
SI 5		*+3*	*Jan18, 2024*	*4*
SI 6		*+4*	*Jan 19, 2024*	*5*
SI 7		*+7*	*Jan 22, 2024*	*5*
SI 8		*+9*	*Jan 24, 2024*	*4*
SI 9		*+11*	*Jan 26, 2024*	*5*
SI 10		*+14*	*Jan 29, 2024*	*4*
SI 11		*+16*	*Jan 31, 2024*	*5*

SI 12		*+21*	*Feb 05, 2024*	*4*
SI 13		*+23*	*Feb 07, 2024*	*5*
SI 14		*+25*	*Feb 09, 2024*	*5*
SI 15		*+30*	*Feb 14, 2024*	*5*
SI 16		*+32*	*Feb 16, 2024*	*4*
SI 17		*+36*	*Feb 20, 2024*	*5*
SI 18		*+39*	*Feb 23, 2024*	*5*
SI 19		*+44*	*Feb 28, 2024*	*5*
SI 20		*+46*†	*Mar 1, 2024*	*5*
SP21	*PI*	*+50*	*Mar 5, 2024*	*5*
SP 22		*+53*	*Mar 8, 2024*	*5*
SP 23		*+57*	*Mar 12, 2024*	*5*
SP 24		*+60*	*Mar 15, 2024*	*5*
SP 25		*+184*	*July 17, 2024*	*5*
Total sampling campaigns: 25			***Total samples: 116***	

*Note: *First sampling day of the injection campaign; †Last sampling day of the injection campaign. CO_2 injection stopped on Mar 2, 2024.*

The samples were collected with a syringe immediately after stabilization of the physicochemical parameters (temperature, pH, EC, ORP and DO), filtered through a 0.22 µm hydrophilic acetate filter (to retain the colloidal material), and transferred to 50 mL polypropylene (PP) Falcon-type tubes or 10 mL Exetainer® vials. For the analysis of dissolved metals (cations plus trace metals), the samples were acidified with 50% HNO_3 in the field until the pH was ≤ 2 and stored at ≤10°C using a portable cooler. For anion analysis, samples underwent only filtration without acidification.

Chemical analyses were performed either at the IPR's Laboratory for Chemical Analysis (LAQ) at PUCRS or at NSF Laboratories Brasil. Anions were analyzed with a Thermo Scientific® Dionex ICS-5000 Ion Chromatograph (IC), while metals were analyzed with an Optima 7000 DV Inductively Coupled Plasma Optical Emission Spectrometer (ICP–OES) from Perkin Elmer®. Analytical errors generally varied from 0.004 to 0.03 mg/L, as determined from duplicate analyses performed for every 20 samples. On the basis of a multielemental standard used for the analysis, the limit of quantification (LOQ) varied across parameters, reaching 0.3 µg/l (for toxic metals such as Cr and Cd) and 0.01 mg/L (for nonmetals and metals). In some cases, the LOQ value was conventionally replaced by LOQ/2 for quantitative interpretation. The aforementioned sampling procedures and analyses are accredited according to ISO/IEC 17025:2017 by the ANSI National Accreditation Board (ANAB) under certificate number AT-3169.

Carbon stable isotope ($^{13}C/^{12}C$) analyses were performed using a GasBench II system coupled to a Delta V Plus isotope ratio mass spectrometer (IRMS) from Thermo Scientific®. Calibration was conducted using the NBS18 primary standard, anchored to the VPDB reference scale (NBS18 = -5.014‰ VPDB) as established by Friedman et al., (1982) and Coplen et al. (2006). The results are expressed as the ratio of the heavy isotope (^{13}C) to the light isotope (^{12}C) in the sample relative to the corresponding ratio in the calibration standard. The isotopic composition of dissolved inorganic carbon (DIC) in water samples is reported as $\delta^{13}C$-DIC per mil (‰). The average analytical precision for these measurements was ± 0.2‰.

Errors in charge balance (CBE), chemical speciation of solutes, partial pressure of CO_2 (PCO_2) and mineral saturation index (SI) calculations were performed using PHREEQC INTERACTIVE 3.7 (Parkhurst and Appelo 2013). The average CBE was -1.4% (20.2% maximum; 0.1 minimum), and those above 10% (only 7 samples) were discarded and not considered in further statistical evaluation, as shown in the discussion section. Hydrochemical graphs and geochemical diagrams were generated by using Plotly or WQChartPy Python libraries (Yang et al., 2022). PCA was accomplished using the freely available *pca* Python package (Taskesen, 2020). Spearman's nonparametric correlation analysis was conducted after confirming the nonnormal distribution of selected representative data using the Shapiro–Wilk test ($p \leq 0.05$). No data transformations were applied, and the correlation coefficient is represented by the Greek letter ρ (Conover, 1999; Shapiro and Wilk, 1965).

To quantify the percentage increase in the monitored hydrochemical parameters (discussed in section 4.3) relative to the natural variability observed over a three-year period at the study site, as reported by Zielinski et al. (2024), the following equation was applied:

$$Parameter\ Variation\ (PV, in\ \%) = \left(\frac{[Ci]CO_2 - [C_i]\ UCL\ or\ LCL}{[Ci]_{UCL\ or\ LCL}}\right) \times 100 \quad (1)$$

where $[Ci]CO_2$ represents the concentration of the i^{th} parameter during the CO_2 injection campaign, and [Ci]UCL or LCL represents the concentration of the respective i^{th} parameter during the 3-year long natural background. The LCL and UCL represent the average calculated for the respective hydrostratigraphic unit minus or plus two times the observed standard deviation, respectively. This equation was adapted from the methodology of Choi et al. (2017), who assessed the sensitivity of groundwater parameters to seasonal variability using the relative standard deviation (RSD). In that framework, parameters with RSD values less than 10% were considered relatively stable, whereas those with values greater than 10% were regarded as sensitive to seasonal fluctuations.

Here, the original concept was modified by evaluating deviations relative to the lower and upper control limits (LCL and UCL) rather than relative to the immediate background concentration, following the monitoring framework established by Zielinski et al. (2024). Furthermore, unlike the approach proposed by Choi et al. (2017), PV values consistently equal to or greater than 20% during the advanced stage of the CO_2 injection phase (injection rate $\geq$ 10 kg day^{-1}) were classified as sensitive to CO_2 leakage. The 20% threshold was selected to distinguish sustained injection-related perturbations from natural hydrochemical variability and short-term fluctuations, ensuring that only persistent and operationally relevant deviations were identified as potential leakage signals.

3. Results

The results from field measurements and laboratory analyses of the collected water samples are comprehensively summarized in Tables S1, S2, and S3. For additional details and a thorough dataset, please refer to the Supplementary Material.

3.1. Temporal evolution of physicochemical parameters

The monitoring of temperature, pH, EC, DO, and ORP started on January 8, proceeded regularly during injection (which started only on January 15 and ended on 3 March), was concentrated in the immediate postinjection, and was measured for one last time on July 17 after a long period of intense rainfall. An immediate background showed that during this period, the pH varied from 5.4 (M3B) to 6.5 (M4B), the EC ranged from 190 µS/cm (M3B) to 493 µS/cm (M4B), the DO concentration ranged from 1.6 mg/L (M1B) to 4 mg/L (M3B), and

the ORP ranged from +202 mV (M3B) to -190 mV (M4B), as shown in Figure 4. The temperature varied from 23.9°C (M4B) to 26.3°C (M2B) and remained within this range for the whole duration of the concentrated field experiment, except for the last postinjection sampling campaign, which took place during the winter when the temperature was lower than 19°C. During this period, the pH decreased for all wells but remained within the observed range for the previous long background campaign carried out for 3 years (Zielinski et al. 2024). This is also true for all the other physicochemical parameters, which experienced some high-amplitude changes before CO_2 was released.

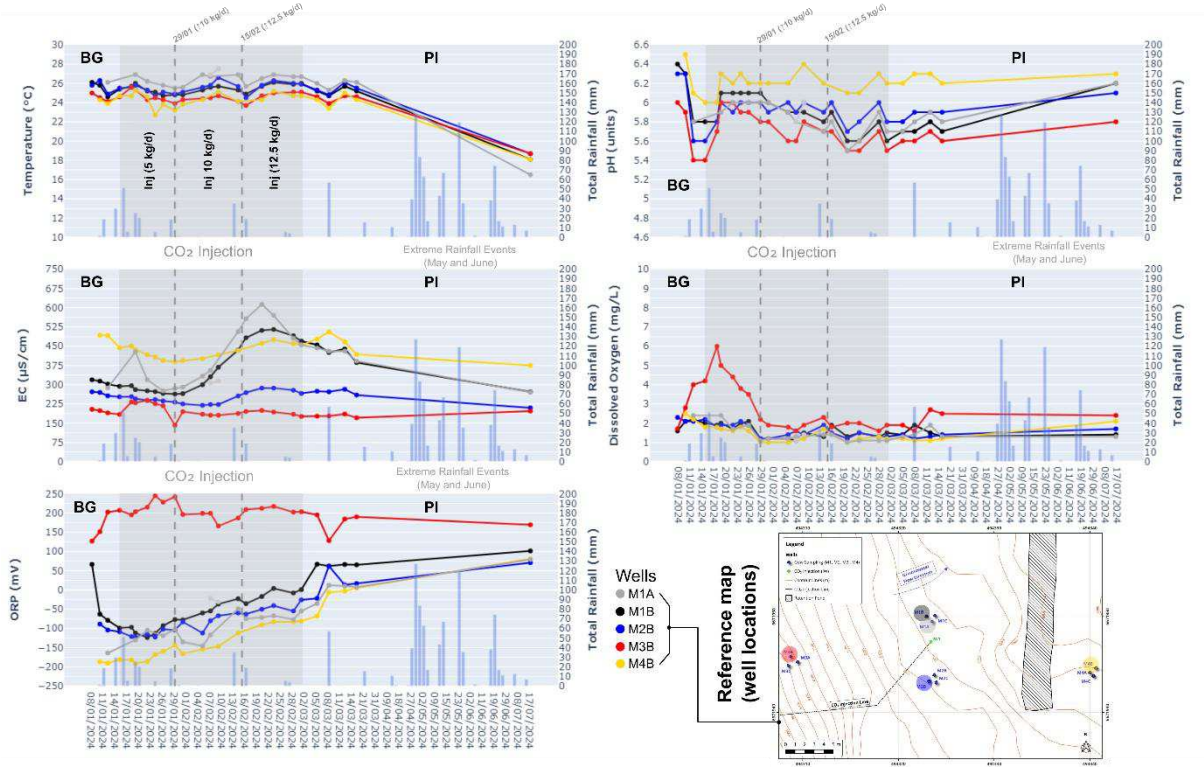


Fig 4 Evolution of physicochemical parameters across different phases: background, CO_2 injection, and postinjection (immediate and long-term). The gray shaded area represents the CO_2 injection phase. The vertical dotted lines indicate the increase in the CO_2 injection rate on January 29 (10 kg/day) and February 15 (12.5 kg/day). BG and PI indicate the background and postinjection phases, respectively

After CO_2 injection started, the pH slightly increased until January 19 and remained nearly constant for all wells until January 29 (14 days after CO_2 began to be released into the aquifer). It showed an observable decrease only after January 31, two days after the decision to increase the injection rate from 5 to 10 kg/day had been made. During this period, the pH decreased from 6 to 5.5 for M1A, from 6.1 to 5.6 for M1B, and from 6 to 5.7 for M2B, the closest to the injection well, with some slight rebounds. This event coincided with breakdowns in the CO_2 injection system on February 5 and 8 and with two precipitation events that resulted in an accumulated amount of ~54.3 mm. M3B showed a decrease in pH from 6 to 5.5 five days earlier, but apparently without any connection to CO_2 injection, as will be seen later. M4B oscillated from 6 to 6.4 units throughout the injection period. The electrical conductivity increased simultaneously, with values rising from 285 µS/cm on January 29 to 613 µS/cm on February 20 for M1A (115% increase) and from 264 µS/cm to 515 µS/cm on February 23 for M1B (95% increase). The EC of well M2B started to increase only on February 14 and reached its highest point on February

23, although its percentage increase was lower than that of the other two wells (an increase of 28.6%). The EC for M4B also started to increase on January 29 but continued to increase slowly until March 8 (29.7% increase).

The DO concentration began to decrease after CO_2 injection for all wells, even for M3B, which increased immediately before the injection started, although not uniformly across wells. From January 15 to January 26, the DO concentration ranged from 1.8 to 2.1 mg/L. On January 29, the concentration decreased to 1.1 mg/L and remained lower than 1.5 mg/L until the end of the injection phase. Minor rebounds to higher levels were observed after February 9, which coincided with periods of heavier rainfall and injection malfunctions. In general, the ORP began to increase seven days after the beginning of CO_2 injection for all wells except for M3B, which oscillated between +166 and +245 mV. Nonetheless, for M1A, M1B, M2B, and M4B, the ORP started to gradually increase on January 22 from a reduction condition (< -120 mV) toward higher ORP values at the end of the injection campaign (between +1 and -81 mV), reaching oxidizing conditions at the end of the postinjection phase.

3.2. Alkalinity and PCO_2 behavior

The evolution of total alkalinity (measured as mg/L of CaCO3) and CO_2 partial pressure (PCO_2, in atm) can be observed in Figure 5. During the background period, the alkalinity of M1A, M1B, and M2B varied from 100.6 to 135.2 mg/L, whereas for M3B, it remained between ~28.0 and 47.1 mg/L, and for M4B, it remained between 218.7 and 249 mg/L. During CO_2 injection, these values initially increased between January 15 and January 19 for M1A and M3B, promoting increases of approximately 38.5% and 115%, respectively. This is possibly linked to the 132.6 mm of rain that accumulated between January 8 and the sampling date, which may have washed down naturally produced CO_2 from soil microbial activity and organic matter degradation. This process can lead to a decrease in pH even as the total alkalinity increases because of a concurrent increase in cations released from mineral dissolution and bicarbonate (HCO_3^-) formation (Lasaga 1984; Drever 1997). Stumm and Morgan (1996) reported that once the buffering capacity is overwhelmed, the pH decreases despite increasing alkalinity, which could explain this observation. Afterward, the total alkalinity began to decrease even when CO_2 injection was still occurring. This was not clearly observed in the other wells.

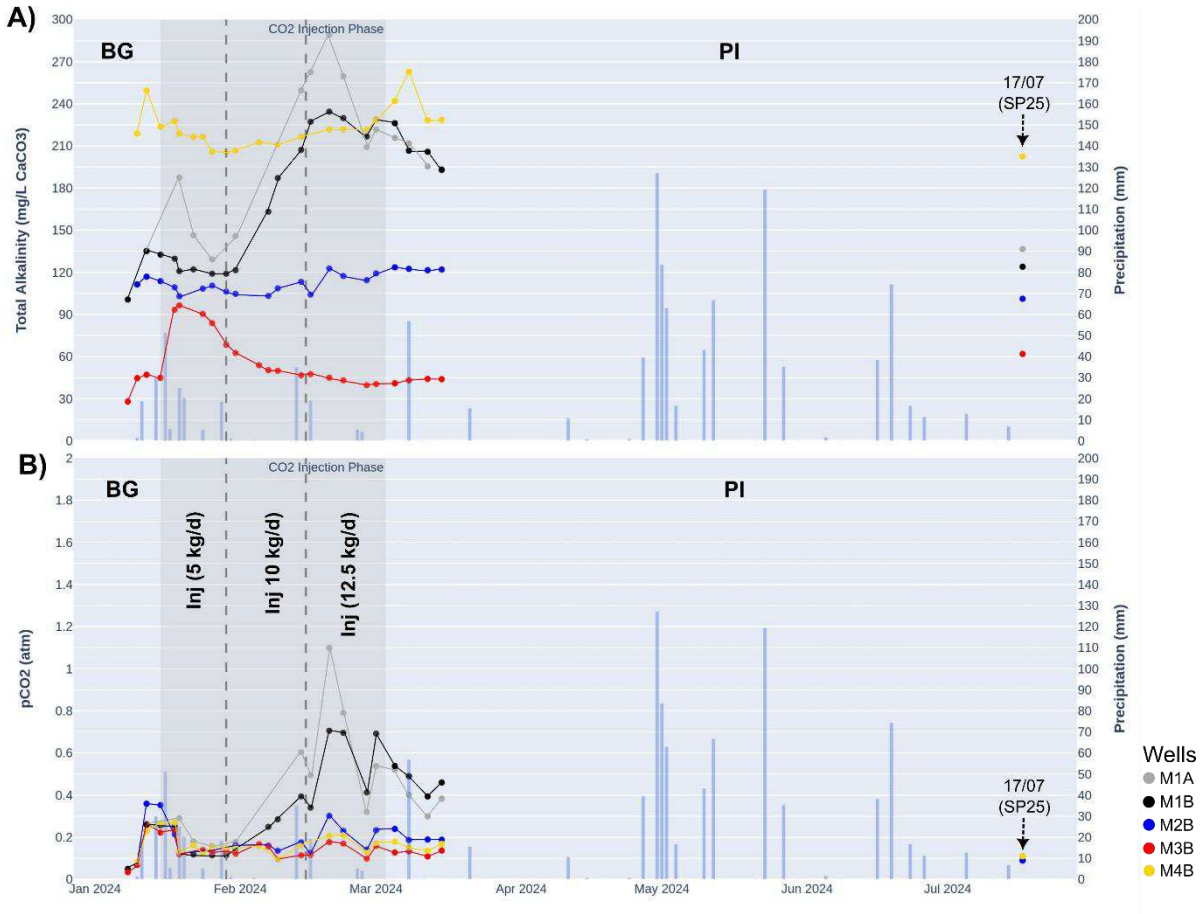


Fig 5 Evolution of total alkalinity (measured in mg/L as CaCO3) and partial pressure of CO_2 (in atm) across the background, CO_2 injection, and postinjection (immediate and long-term) phases. The gray shaded area indicates the CO_2 injection phase. The vertical dotted lines indicate the increase in the CO_2 injection rate on January 29 (10 kg/day) and February 15 (12.5 kg/day). BG and PI indicate the background and postinjection phases, respectively

No significant changes were measured in wells M1B and M2B until the injection rate increased to 10 kg/day and later to 12.5 kg/day. On January 26 and 31, the total alkalinity started to increase from 129.2 to 289.2 mg/L (an almost 124% increase) for M1A and from 121.5 to 234.4 mg/L (an almost 92.3% increase) for M1B, respectively. This level of change clearly occurred only in these two wells during the most advanced phase of CO_2 injection (a release rate of 12.5 kg/d), as the alkalinity of M3B continuously decreased throughout the experiment, whereas that of M4B increased by only 24% after 9 February, suggesting that the flow path of the CO_2-charged groundwater had not affected these wells.

In addition, the PCO_2, which varied from 0.03 to 0.35 atm during the background and initial injection phases for all the wells in general, sharply increased to approximately 1.1 atm (M1A) and 0.7 atm (M1B) on February 20, a growth of 541% and 545%, respectively. After this period, the value started to decrease but remained above the levels observed in the background phase during immediate postinjection, suggesting possible residual dissolved CO_2 in the sampled groundwaters because of slower re-equilibration. Apart from M2B, which showed somewhat similar but more subtle behavior, the PCO_2 values for wells M3B and M4B varied within a restricted interval and did not clearly increase.

3.3. Dissolved ion time series trend

The observed changes in dissolved ions aligned with the evolution of physicochemical parameters, such as alkalinity and PCO_2, as CO_2-affected groundwater progressed through the field. As illustrated in Figure 6, the concentrations of Ca, Mg, K, Na, Sr, Ba, Fe, and Si gradually increased in wells M1A and M1B during CO_2 injection, particularly after the injection rate was increased to 10 kg/day and subsequently to 12.5 kg/day. The concentration peaked on February 20 or 23 (depending on the parameter) and then began to decline progressively. However, they did not return to background levels within two weeks post-injection, with recovery occurring in the weeks following the final immediate postinjection sampling campaign (SP24), as confirmed by the subsequent SP25 campaign. The manganese (Mn) concentrations in these wells exceeded the quantification levels only after February 20, with values of 0.14 and 0.11 mg/L for M1A and M1B, respectively. Although the Mn concentrations in M1A decreased to low levels, they remained above 0.1 mg/L (100 µg/L) in M1B.

The concentrations of some parameters (Ca, Mg, K, Na, Fe, and Si) in well M2B also increased, although less consistently as they did in the previously discussed wells. Additionally, chemical species such as Ba and Sr did not noticeably increase. The manganese (Mn) concentrations in M2B peaked during the same period as those in M1A and later decreased to low levels. In well M3B, the concentrations of Ca, Mg, K, Sr, Na, and Si initially sharply increased during the background or low injection rate period but subsequently decreased even during CO_2 injection, indicating a possible lack of correlation with the injection process. Finally, the concentration levels in M4B exhibited either oscillating behavior or a relatively stable pattern with no apparent relationship to the progression of CO_2 injection, which is consistent with the initial assumption that this well functioned as a distal/unimpacted reference during the test.

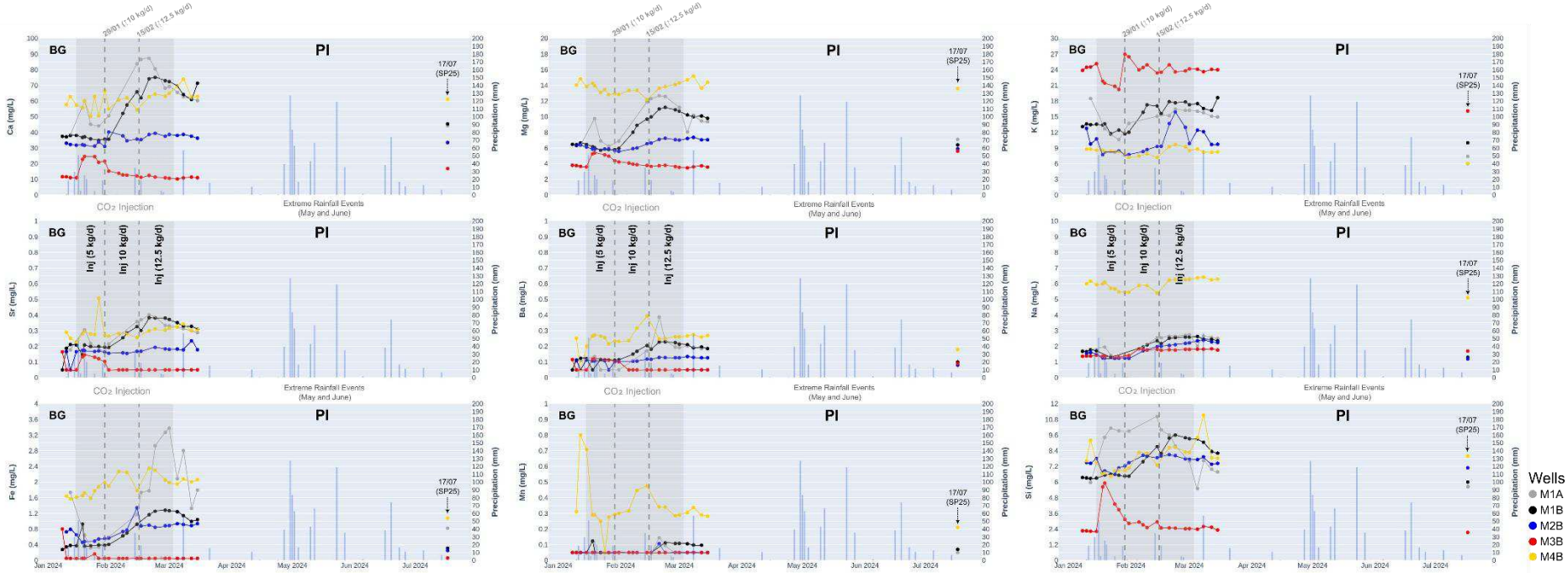


Fig 6. Time series of dissolved cation concentration trends for the sampled wells throughout the experimental period. The gray shaded area denotes the CO_2 injection phase. The vertical dotted lines mark the increases in the CO_2 injection rate on January 29 (to 10 kg/day) and February 15 (to 12.5 kg/day). BG and PI indicate the background and postinjection phases, respectively

Additionally, the Cl^- and HCO_3^- concentrations exhibited patterns similar to those of the cations in wells M1A and M1B, with a gradual increase during CO_2 injection (Figure 7). However, a similar Cl^- behavior was also observed in wells M2B and M4B, while HCO_3^- consistently followed the trend of major cations across all the wells. Phosphate (PO_4^{3-}) generally remained at low levels in wells M3B and M4B but showed a notable peak in wells M1A, M1B, and M2B during the initial days of CO_2 injection, until the injection rate was increased to 10 kg/day, after which it began to decline.

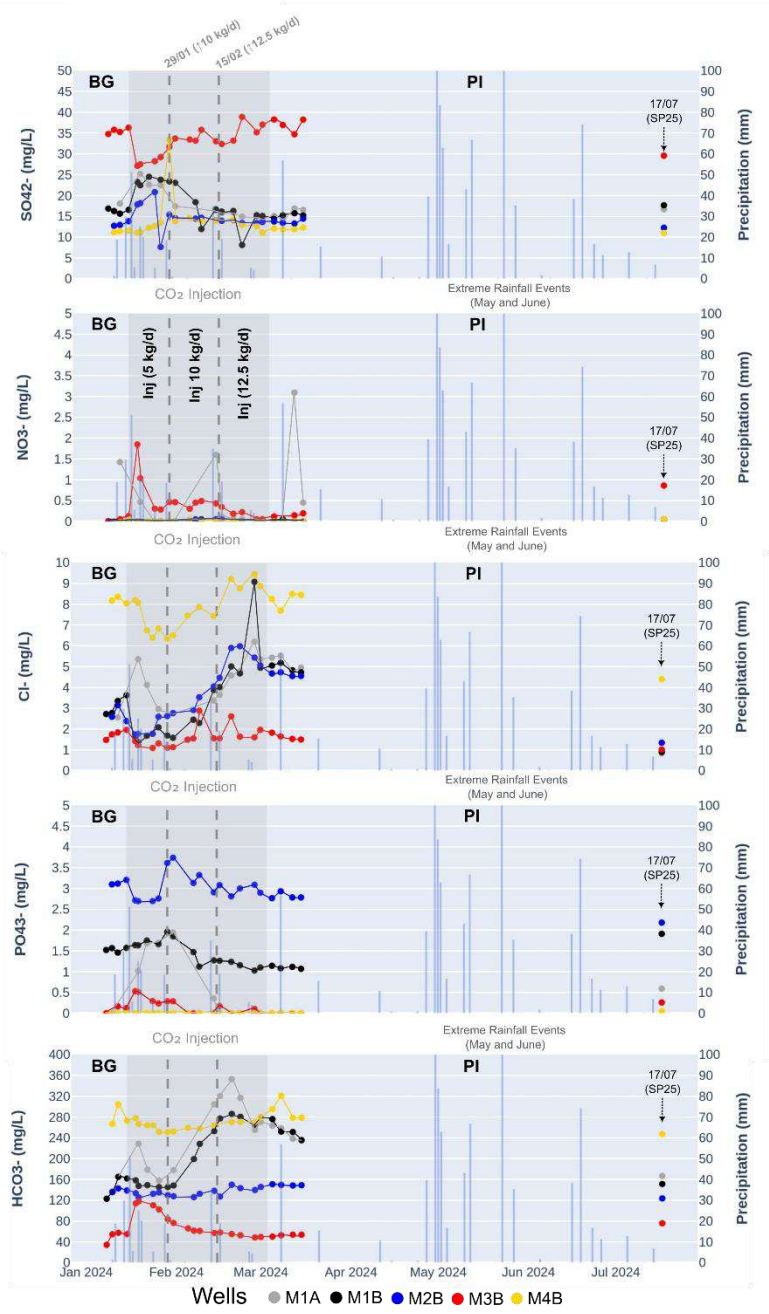


Fig 7 Time series of dissolved anion concentration trends for the sampled wells throughout the experimental period. The gray shaded area denotes the CO_2 injection phase. The vertical dotted lines mark the increases in the CO_2 injection rate on January 29 (to 10 kg/day) and February 15 (to 12.5 kg/day). BG and PI indicate the background and postinjection phases, respectively

Sulfate (SO_4^{2-}), in contrast, initially increased during the early stages of CO_2 injection but subsequently decreased in wells M1A, M1B, and M2B as the injection progressed. In well M3B, SO_4^{2-} progressively increased after an initial decrease at the beginning of CO_2 injection, whereas in well M4B, SO_4^{2-} exhibited minimal change. Nitrate (NO_3^-) concentrations displayed an irregular pattern across all wells throughout the experiment, with sudden increases followed by sharp decreases that appeared unrelated to CO_2 release in the aquifer. However, the peaks observed in well M1A occurred immediately after significant precipitation events. All other dissolved ions, such as Al, B, Cd, Pb, Co, Cu, Cr, Li, Ni and Zn, either were not detected (below the limit of detection) or remained below the LOQ.

3.4. Mineral saturation indices

The mineral saturation indices (SI) for wells M1A and M1B are presented in Figure 8. The data indicate that the SI values reached their lowest levels on January 12 (M1A) and January 15 (M1B) for the oxide and oxyhydroxide phases ($Al(OH)_3$(a), Al_2O_3, $Fe(OH)_3$(a), gibbsite, goethite, and lepidocrocite), immediately preceding a series of three precipitation events during the final background campaigns and the initial days of low injection rates. Following this period and a short subsequent small increase in the SI, the aluminum-rich phases $Al(OH)_3$(a), Al_2O_3 and gibbsite slightly decreased in the SI, indicating a tendency toward dissolution as CO_2 injection commenced and as the injection rate increased to 10 kg/d.

After the peak in PCO_2, the SI values for these phases began to return to preinjection conditions. In contrast, iron-rich phases such as $Fe(OH)_3$(a), goethite, and lepidocrocite demonstrated a progressive increase in the SI, moving toward saturation, which suggests a shift in hydrochemical conditions that favor precipitation. However, among these, only gibbsite actually achieved an SI > 0. Although there were occasional oscillations in the SI values, the overall trend remained clear.

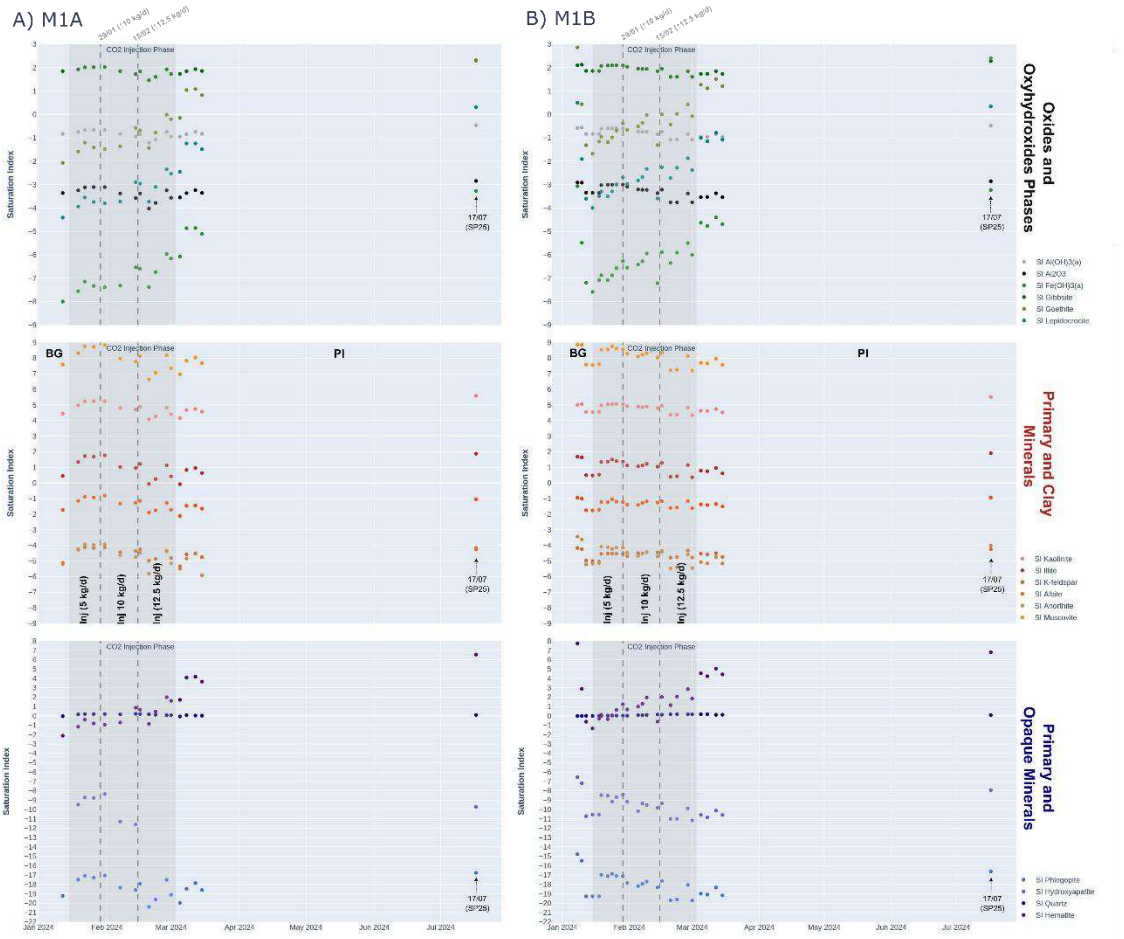


Fig 8 Observed trends and patterns in the saturation indices (SI) of secondary minerals, oxyhydroxide phases, and primary minerals observed during the CO_2 injection experiment in wells M1A (A) and M1B (B)

Primary and clay minerals exhibited a progression in their SI toward conditions more conducive to precipitation—either increasing favorability or indicating shifts in environmental conditions that would facilitate this process—until January 31. Following this date, a consistent decrease in the SI was observed after the CO_2 injection rate increased to 10 kg/day, which continued until February 20, at which point the SI values began to return to preinjection levels. This trend was observed in both M1A and M1B, with a more pronounced response in M1A. Muscovite, kaolinite, and illite predominantly remained in the supersaturated field (SI > 0), whereas K-feldspar, albite, and anorthite experienced increasingly negative SI values, suggesting that these minerals were actively dissolving and releasing their constituent elements into the groundwater.

Phlogopite (used here as a thermodynamic representation for biotite) and hydroxyapatite also followed this pattern, shifting toward conditions that favor dissolution as CO_2 injection progressed to higher levels. In contrast, quartz remained largely unaffected, whereas hematite (used as a proxy for a kinetically slow oxide phase) transitioned from undersaturated to supersaturated conditions during the CO_2 injection phase and remained above SI > 0 until the final postinjection sampling campaign.

These results suggest that secondary phases such as $Fe(OH)_3(a)$, goethite, lepidocrocite, kaolinite, and illite, along with primary minerals such as K-feldspar, albite, anorthite, muscovite, biotite, and hydroxyapatite, exhibited changes in their SI trends as CO_2 injection progressed. This behavior could be

interpreted as indicating that these minerals act as sources of elements whose concentrations increase in response to CO_2 injection.

3.5. Evolution of the stable carbon isotopic signature of groundwater (δ^{13}C-DIC)

The carbon isotopic composition of dissolved inorganic carbon (δ^{13}C-DIC, ‰) was monitored throughout the experiment. During the injection phase, the δ^{13}C-DIC values of wells M1A and M1B sharply decreased from approximately -9‰ to -7‰ and reached values near -30‰. This trend indicates a strong influence of the injected CO_2, whose isotopic signature of δ^{13}C-CO_2 is equal to -38.5 ± 2.5‰ (Figure 9). A marked inflection in δ^{13}C-DIC was observed when the injection rates were increased to 10 and subsequently 12.5 kg/d. In contrast, wells M2B, M3B, and M4B maintained relatively stable δ^{13}C-DIC values between -4‰ and -12‰, in addition to being rare outliers. These values remained within the previously characterized seasonal background range for each well (Zielinski et al., 2024), suggesting minimal or negligible influence from the injected CO_2, which is consistent with a limited plume reach.

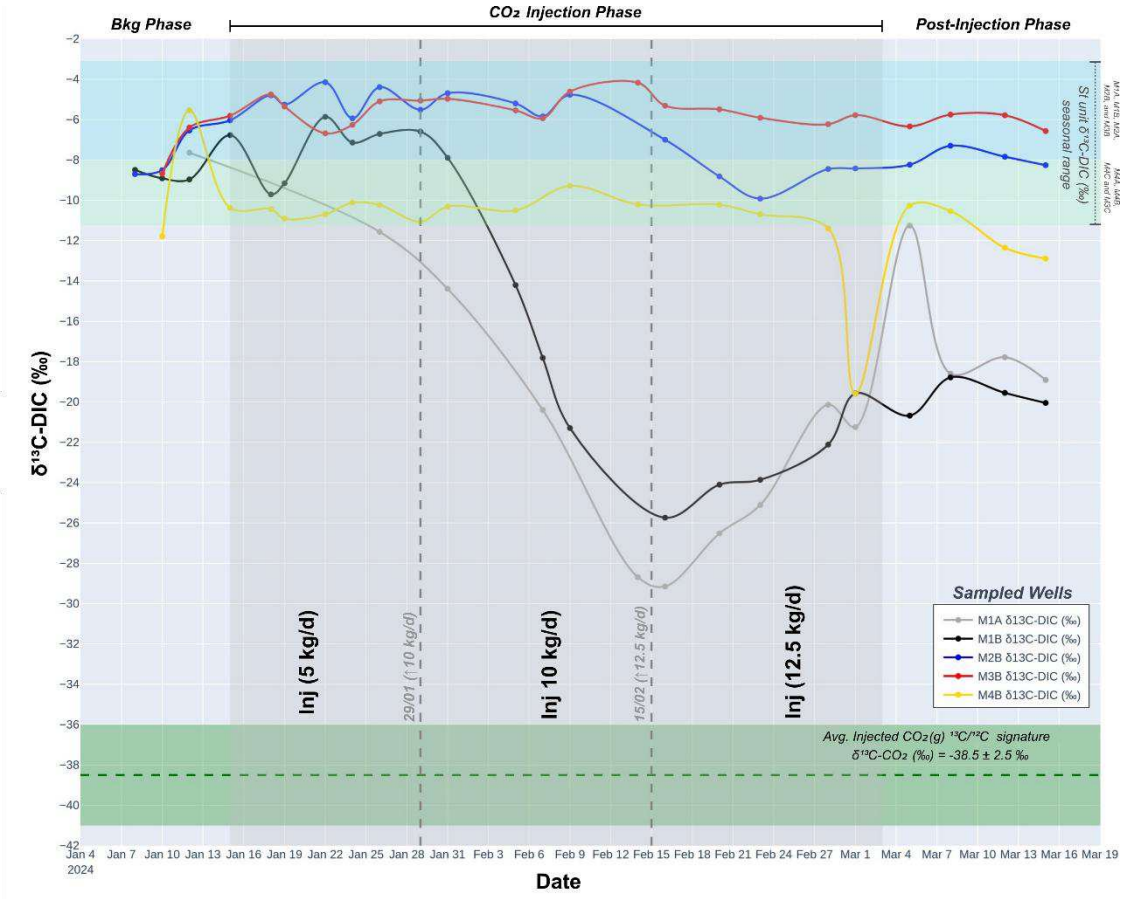


Fig 9 Evolution of carbon isotopic composition (δ^{13}C-DIC) in monitored groundwaters during the background (Bkg), injection, and postinjection phases. Light blue and green rectangles indicate the range of seasonal variation observed during long-term (>3 years) natural monitoring of the St unit (sampled interval) for each well group

4. Discussion

The results are discussed using a three-tier framework. Tier 1 consists of PCA, which serves as a key tool for identifying the variables that contribute most strongly to the differentiation between impacted and unimpacted wells. Tier 2 comprises correlation analyses with pCO_2, highlighting variables that are both structurally important in the multivariate dataset and statistically associated with CO_2 and quantitatively describing the strength of these relationships. Finally, Tier 3 focuses on the variables that exhibit the strongest correlations with pCO_2 during the controlled CO_2 release experiment, providing evidence of responses that are linked to CO_2 perturbation, persist or recur beyond short-term variability, and remain distinguishable from natural background fluctuations regarding the three-year-long study conducted in our previous publication (Zielinski et al. 2024).

4.1. PCA and CO_2-impacted groups

To manage the large number of variables, the initial step involved reducing the dimensionality of the dataset with minimal loss of information. This analysis was conducted using principal component analysis (PCA, Jolliffe, 1986) on all chemical species with significant concentrations (Ca, Mg, K, Na, Fe, Si, HCO_3^-, SO_4^{2-}, Cl^-, NO_3^-, PO_4^{3-}, Ba, Sr, and Mn), physicochemical field measurements (temperature, EC, DO, pH, and ORP), and total alkalinity, PCO_2 and δ^{13}C-DIC. This approach has been shown to be effective, as demonstrated by DO Do et al. (2020). According to Figure 10a, wells M3B and M4B are clearly clustered separately from wells M1A, M1B, and M2B (and from each other) according to PC1 and PC2, which collectively account for ca. 68.7% of the total explained variance from the dataset. Additionally, they are homogeneously grouped and do not show any evident dispersion after CO_2 injection.

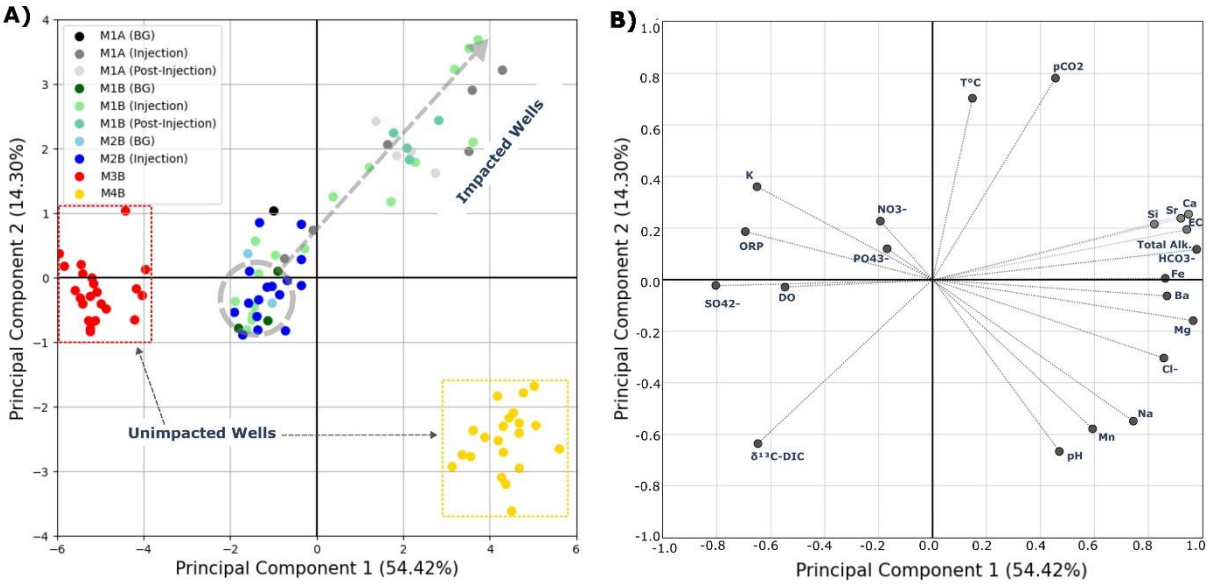


Fig 10 PCA of all groundwater samples collected during background, CO_2 injection and postinjection: a) segmented groups based on scores of water samples by PC1 and PC2; and b) loadings of evaluated variables and their respective eigenvectors

Conversely, wells M1A, M1B, and M2B are clearly differentiated. While M2B remains primarily concentrated between PC1-2 to 0 and PC2-1 to +1, even during CO_2 injection, background data from wells M1A and M1B indicate initial concentrations between PC1-2 to 0 and PC2-1 to 0 (dashed gray circle) but

display regular data dispersion toward the upper right quadrant (dashed gray arrow), clearly indicating the influence of CO_2 as injection progresses.

After the loadings and eigenvectors were computed (Figure 10b), the evolution of CO_2-impacted wells was observed to be positively correlated primarily with total alkalinity/HCO_3^-, EC, Mg, Ca, Sr, Fe, Ba, Cl^-, and Si and secondarily with Na, Mn, PCO_2, and pH. In contrast, NO_3^-, PO_4^{3-} (to a lesser extent), DO, K, ORP, SO_4^{2-}, and δ^{13}C-DIC negatively contributed to the progression of the impacted group. Additionally, PCO_2 is relatively weakly correlated (<90°) with Si, Ca, Sr, and HCO_3^- and with total alkalinity, EC, Fe, Mg, Ba, Cl^-, pH, Na, and Mn, indicating a positive correlation, whereas it was positively correlated with δ^{13}C-DIC, suggesting an inverse relationship. These results indicate that PCO_2 may serve as a proxy for characterizing CO_2 interactions in impacted wells and their expression in terms of hydrogeochemical variables.

4.2. Correlation analysis and PCO_2 vs. dissolved ion evolution path

To assess the extent of the impact of CO_2 injection on the evaluated hydrochemical variables and identify those most strongly associated with this process, a correlation analysis was performed using Spearman's correlation coefficient (SCC). This analysis examined the relationships between PCO_2 and twenty variables, including EC, DO, pH, ORP, total alkalinity, Ca, Mg, K, Na, Fe, Si, HCO_3^-, SO_4^{2-}, Cl^-, NO_3^-, PO_4^{3-}, Ba, Sr, Mn and δ^{13}C-DIC. As noted by Do et al. (2022), although PCO_2 cannot be directly used in this case as a tracer for diagnosing CO_2 leakage, since it is an indirect parameter calculated using PHREEQC, which uses temperature, pH, alkalinity, and ion concentrations to compute PCO_2-, the advancement of technology enabled the use of PCO_2 sensors to establish a direct correlation more accurately. Hence, we used the calculated PCO_2 as a reference point that could be quantitatively anchored with a sensing device, although this was not the focus of this study.

As shown in Table 3, which was constructed considering only the parameters monitored during the CO_2 injection phase, M1A and M1B had the greatest number of variables strongly correlated with PCO_2 ($\rho >$ 0.60), whereas most of the parameters for M2B had a weak (0.20 to 0.39) to moderate (0.40 to 0.59) correlation, with some exceptions (Weir 2014). On the other hand, in both M3B and M4B, most variables exhibited either very weak or no correlation (0.00 to 0.19). In this context, a more stringent statistical threshold was applied by restricting the analysis to variables with correlation coefficients greater than 0.70, even though the literature typically considers values above 0.60 as indicating strong correlations. Using these stricter criteria, the variables identified as strongly correlated in both M1A and M1B were EC, pH, ORP, total alkalinity, Ca, Mg, K, Na, Fe, HCO_3^-, PO_4^{3-}, Ba, Sr, and δ^{13}C-DIC.

The correlations of other variables, such as Si, SO_4^{2-}, and Cl^-, were stronger in M1B than in M1A, indicating a relatively weaker relationship between these variables and PCO_2 in the shallower interval. This suggests that another factor weakened the correlation, which we interpret to be the influence of rainfall, as will be further discussed. The correlation coefficients obtained for EC, pH, Ca, Mg, Na, K, Sr, Ba, Si, Mn and δ^{13}C-DIC are of the same order of magnitude or are closely comparable to those reported by Do et al. (2022) for the most impacted well in their study. This agreement is noteworthy given the similar geological settings of both studies, which involve granite-derived shallow aquifer systems, and despite the use of

Pearson's correlation method by Do et al. (2022). An exception is Li, which was not detected above the minimum quantification level in this study.

Table 3. Spearman's correlation coefficient (SCC) for PCO_2 and the corresponding variables according to the degree of CO_2 impact: a) M1A and M1B are highly impacted wells; b) M2B is moderately impacted; and c) M3B and M4B are considered unimpacted wells.

	EC	DO	pH	ORP	Total Alk.	Ca	Mg	K	Na	Fe	Si	HCO_3^-	SO_4^{2-}	Cl^-	NO_3^-	PO_4^{3-}	Ba	Sr	Mn	$\delta^{13}C$-DIC
M1A	**0.94**	-0.64	**-0.99**	**0.83**	**0.93**	**0.90**	**0.96**	**0.72**	**0.76**	**0.70**	-0.22	**0.93**	-0.62	0.36	0.57	**-0.81**	**0.88**	**0.94**	**0.70**	**-0.72**
M1B	**0.94**	-0.20	**-0.89**	**0.82**	**0.97**	**0.95**	**0.96**	**0.90**	**0.93**	**0.83**	**0.84**	**0.97**	**-0.85**	**0.83**	0.23	**-0.85**	**0.90**	**0.86**	0.61	**-0.71**
M2B	0.37	-0.06	**-0.89**	0.41	**0.74**	0.50	0.46	0.50	0.42	0.39	0.37	**0.74**	-0.36	0.30	-0.00	-0.06	0.50	0.20	0.37	-0.20
M3B	0.11	0.36	-0.54	0.26	0.00	0.04	0.01	0.09	-0.01	0.03	-0.06	0.00	0.06	0.07	-0.22	0.00	0.04	0.08	NC	-0.30
M4B	0.49	0.07	**-0.89**	0.07	0.66	-0.15	0.28	0.50	0.35	-0.11	0.18	0.66	-0.31	0.38	0.32	NC	-0.18	-0.05	0.29	-0.17

By plotting the variables against PCO_2 on a scatterplot and considering the chronological sequence of the sampling procedures alongside the incremental increase in injection rates, an evolutionary trend can be clearly identified for some parameters in the most impacted wells (Figure 11). As shown in Figure 11a (well M1B), the major cations Ca, Mg, K, Na, and Si, along with the elements Fe, Ba, and Sr, and the bicarbonate anion (HCO_3^-), clearly increase from their baseline concentrations, or even during the low CO_2 injection rate of 5 kg/day, which is concentrated within the lower left quadrant of each graph. These concentrations increase with the injection rate, reaching peak levels at 12.5 kg/day in the upper right quadrant. After this peak, the concentrations begin to return to baseline levels during the postinjection phase, ultimately approaching the cluster of background or nearly unaffected water compositions (lower left corner).

Manganese (Mn) remains below or near the limit of quantification (LOQ) most of the time, except when the injection rate is increased to 12.5 kg/day. At this rate, its concentration increased by more than 100%, reaching detection levels greater than 0.1 mg/L (100 µg/L). A less clear correspondence is observed with SO_4^{2-}, Cl^-, and PO_4^{3-}, where a clear trend is not readily apparent, although an evolutionary path can be discerned. While SO_4^{2-} and PO_4^{3-} decreased with increasing PCO_2, Cl^- levels increased slightly as the injection progresses.

Although M1A is clearly impacted, its evolutionary trend is not as distinct as that of M1B (Figure 11b). In this case, Ca, Mg, K, Na, Si, Fe, Ba, Sr, and HCO_3^- exhibit more scattered distributions during background and low release rates, complicating the analysis. Even though their concentration levels increased as PCO_2 was increased, a clear positive correlation was not clearly established, and sometimes a more complex pathway was needed to explain evolution. For example, the highest Fe concentration in M1A was reached after the peak was attained for the other parameters, whereas Si reached its highest concentration earlier than the other variables did. For SO_4^{2-}, Cl^-, and PO_4^{3-}, their behavior was even more intricate, and the traced evolution is nearly indistinguishable. The graphs for M2B, which displays a less distinct evolutionary pathway, as well as those for M3B and M4B, which show a scattered relationship between PCO_2 and the evaluated variables, are presented in Figures S1, S2 and S3 (Supplementary Material).

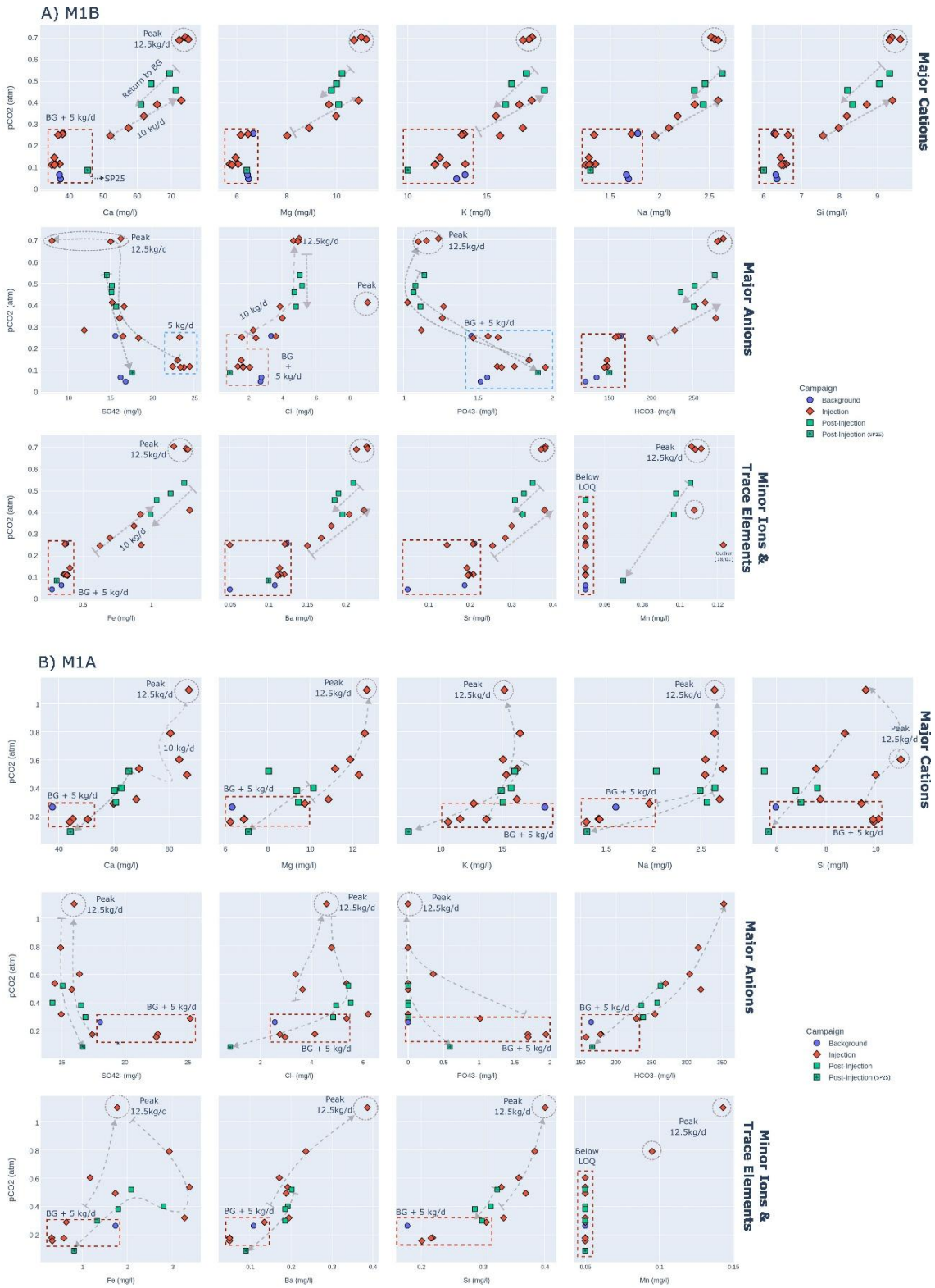


Fig 11 Evolutionary pathway of ion and trace element concentrations during background conditions, low CO_2 injection rates, increasing injection rates, peak levels, and subsequent return to background levels during both the immediate and long-term postinjection phases

4.3. Parameter variation and sensitivity to CO_2 leakage

Although correlation analysis revealed positive or negative associations with PCO_2 (EC, pH, ORP, total alkalinity, Ca, Mg, K, Na, Fe, HCO_3^-, PO_4^{3-}, Ba, Sr, and $\delta^{13}C$-DIC, as shown in the above section), and the evolutionary path during the background, injection and postinjection phases is shown in Figure 11, a leakage episode can be misinterpreted if natural longer-term background variation is unaccounted for (Beaubien et al. 2015; Utley et al. 2023; Wang et al. 2023; Ma et al. 2024). Hence, to avoid considering possible parameters that might be equivocally interpreted as leakage signals, an approach to evaluate sensitivity to CO_2 derived from Choi et al. (2017) was employed (as shown in section 2.2). In this study, PVs that remained consistently equal to or greater than 20% in the advanced stage of the CO_2 injection phase (injection rate ≥ 10 kg/day) were considered to indicate sensitivity to CO_2 leakage (Table 4).

Table 4. Parameter variations (%) of each evaluated variable consistently exhibited either a positive or negative correlation with PCO_2 (wells M1A, M1B and M2B), referenced to the UCL or LCL of the natural background level monitored for at least 3 years prior to the execution of the CO_2 injection experiment.

Well	*Inj. Rate (kg/d)*	*Date*	*Phase*	*Parameter Variation (%)*												
				ΔEC UCL	*ΔpH* LCL	*ΔCa* UCL	*ΔMg* UCL	*ΔNa* UCL	*ΔFe* UCL	*ΔSi* UCL	*ΔHCO₃* UCL	*ΔCl* UCL	*ΔBa* UCL	*ΔSr* UCL	*ΔMn* UCL	*Δ δ¹³C-DIC* LCL
M1A	0	12/01	BG	-14.2	4.6	-7.9	-15.3	-71.4	**38.9**	-46.7	**23.0**	-57.1	-16.3	-15.4	-38.3	**49.0**
	5	19/01		**27.5**	6.2	**46.2**	**30.7**	-65.1	-48.4	-15.8	**70.7**	-10.2	3.9	**45.5**	-38.3	**325.5**
	5	22/01		-4.9	7.0	10.1	-7.6	-74.6	-74.2	-9.6	**33.3**	-31.0	-61.5	4.1	-38.3	-
	5	26/01		-17.7	8.2	7.5	-16.4	-77.0	-73.2	-11.4	17.6	-50.4	-61.5	-4.2	-38.3	**127.5**
	10	31/01		-13.3	6.8	**23.3**	-7.9	-74.5	-52.7	-11.6	**32.8**	-53.7	-61.5	2.8	-38.3	**182.4**
	10	14/02		**51.1**	1.9	**104.2**	**59.3**	-54.5	-6.2	-1.6	**127.1**	-43.5	**32.0**	**70.6**	-38.3	**462.7**
	12.5	16/02	*Injection*	**66.1**	3.6	**111.0**	**64.8**	-54.6	**38.6**	-10.7	**138.9**	-39.0	**44.8**	**76.0**	-38.3	**470.6**
	12.5	20/02		**82.6**	-1.0	**112.8**	**69.8**	-52.8	**42.0**	-14.3	**163.2**	-23.3	**197.8**	**90.9**	**76.7**	**419.6**
	12.5	23/02		**69.9**	0.9	**96.4**	**68.5**	-52.8	**134.2**	-21.8	**136.2**	-20.0	**82.1**	**82.9**	17.5	**392.2**
	12.5	28/02		**43.3**	4.7	**66.3**	**45.5**	-51.9	**161.4**	-30.7	**90.4**	3.8	**50.1**	**58.9**	-38.3	**294.1**
	12.5	01/03		**35.7**	2.1	**68.8**	**49.8**	-51.3	**170.1**	-32.2	**101.8**	-10.2	**48.0**	**57.1**	-38.3	**315.7**
	0	05/03		**32.1**	2.7	**59.8**	7.8	-63.8	**66.8**	-50.9	**96.4**	-9.0	**55.6**	**54.0**	-38.3	**121.6**
	0	08/03		**28.3**	3.0	**53.0**	**36.1**	-52.8	**124.4**	-31.8	**92.7**	-7.6	**48.0**	**49.1**	-38.3	**264.7**
	0	12/03	*PI*	**28.5**	4.9	**48.2**	**26.6**	-54.2	6.3	-37.6	**77.9**	-19.0	**43.1**	**42.1**	-38.3	**249.0**
	0	15/03		16.9	3.9	**47.1**	**25.4**	-55.5	**43.6**	-39.5	**76.0**	-17.0	**43.2**	**36.6**	-38.3	**270.6**
	0	17/07		-19.4	10.8	8.0	-5.0	-76.8	-34.4	-49.4	**24.3**	-86.1	-30.8	-	-38.3	2.0
M1B	0	08/01		-5.0	13.8	-8.8	-13.5	-70.0	-77.9	-43.3	-8.4	-54.4	-61.5	-76.2	-38.3	-4.5
	0	10/01	BG	-6.4	12.4	-9.5	-14.0	-70.3	-72.4	-43.6	1.4	-53.6	-16.7	-10.7	-38.3	0.0
	0	12/01		-10.1	3.3	-7.1	-10.9	-68.3	-69.5	-44.0	**23.1**	-43.9	-4.6	0.7	-38.3	1.1
	5	15/01		-12.3	3.0	-7.3	-13.7	-69.4	-70.3	-43.7	**20.7**	-39.2	-6.6	-1.0	-38.3	-23.6
	5	18/01		-11.8	3.6	-10.4	-17.6	-76.1	-25.8	-40.7	18.0	-73.2	-61.5	-30.9	52.1	9.0
	5	19/01		-16.3	8.9	-9.4	-19.1	-76.0	-71.0	-41.6	10.0	-76.9	-7.4	-0.8	-38.3	3.4
	5	22/01		-17.7	8.6	-12.6	-23.5	-76.9	-70.3	-41.2	11.1	-71.9	-11.1	-5.2	-38.3	-33.7
	5	26/01		-20.6	9.1	-14.9	-22.3	-77.6	-68.6	-41.7	8.3	-65.1	-13.5	-5.7	-38.3	-24.7
	5	29/01		-21.2	8.5	-13.0	-22.4	-77.1	-69.2	-42.3	8.3	-71.7	-13.9	-7.0	-38.3	-25.8
	10	31/01	*Injection*	-21.0	7.7	-13.1	-20.4	-77.1	-67.4	-42.4	10.6	-73.6	-11.8	-8.0	-38.3	-11.2
	10	07/02		-1.4	5.1	**27.0**	7.3	-65.2	-49.9	-32.5	**48.5**	-59.0	16.0	**21.5**	-38.3	**100.0**
	10	09/02		9.6	6.2	**40.1**	19.1	-62.7	-44.1	-28.8	**70.3**	-61.6	**29.7**	**36.0**	-38.3	**139.3**
	10	14/02		**29.6**	4.4	**60.7**	**29.7**	-58.0	-26.4	-22.2	**88.6**	-35.0	**57.6**	**55.3**	-38.3	-28.1
	12.5	16/02		**44.0**	5.4	**51.1**	**33.6**	-61.1	-30.0	-26.9	**106.8**	-32.8	**39.7**	**43.4**	-38.3	**188.8**
	12.5	20/02		**52.5**	0.1	**80.9**	**47.1**	-55.1	-6.8	-16.3	**113.3**	-16.1	**75.1**	**82.2**	**31.3**	**170.8**

	12.5	23/02		**53.5**	0.4	**83.1**	**49.9**	-54.4	0.3	-14.3	**109.2**	-21.7	**76.0**	**81.5**	**37.6**	**168.5**
	12.5	28/02		**46.2**	3.5	**78.0**	**45.7**	-53.8	2.6	-16.1	**97.3**	**52.1**	**72.3**	**81.2**	**33.1**	**148.3**
	12.5	01/03		**40.0**	1.0	**76.6**	**43.2**	-53.8	1.4	-16.8	**108.1**	-17.1	**64.7**	**77.2**	**33.7**	**120.2**
	0	05/03		**35.7**	1.8	**69.5**	**36.8**	-53.1	-0.6	-16.8	**105.8**	-15.3	**61.7**	**67.4**	**30.5**	**132.6**
	0	08/03		**27.0**	2.4	**56.3**	**33.9**	-56.2	-8.6	-19.2	**88.0**	-13.2	**46.8**	**57.5**	**21.1**	**111.2**
	0	12/03	*PI*	**30.9**	2.9	**49.0**	**35.0**	-56.5	-20.4	-25.5	**87.3**	-19.2	**50.7**	**56.1**	19.5	**120.2**
	0	15/03		15.2	2.0	**74.1**	**31.1**	-58.1	-16.8	-26.7	**75.6**	-20.8	**42.9**	**47.0**	-38.3	**124.7**
	0	17/07		-19.0	10.1	10.7	-14.3	-76.8	-75.2	-46.4	12.9	-84.9	-23.1	-	-13.6	-38.2
	0	10/01	*BG*	-19.6	12.1	-19.4	-15.5	-72.3	-41.7	-33.0	1.4	-56.6	-13.4	-20.7	-38.3	14.9
	0	12/01		-23.3	0.1	-21.4	-14.0	-71.5	-36.6	-33.6	6.4	-47.3	-61.5	-76.2	-38.3	-12.2
	5	15/01		-24.6	0.4	-22.5	-17.9	-73.8	-47.8	-30.3	3.5	-60.1	-13.2	-21.0	-38.3	-18.9
	5	18/01		-24.3	3.3	-21.7	-21.5	-77.5	-63.4	-39.8	-0.5	-70.8	-17.4	-16.7	-38.3	-35.1
	5	19/01		-27.0	7.6	-22.7	-21.7	-77.8	-61.8	-38.8	-6.3	-70.4	-18.0	-17.7	-38.3	-28.4
	5	24/01		-28.0	8.1	-23.9	-21.3	-78.0	-60.6	-41.1	-1.3	-70.3	-16.6	-20.6	-38.3	-20.3
	5	26/01		-29.5	6.8	-17.7	-21.3	-77.8	-56.4	-36.8	0.6	-56.6	-61.5	-18.5	-38.3	-40.5
	5	29/01		-31.0	8.2	-24.3	-23.9	-77.8	-55.4	-35.4	-3.3	-56.1	-21.7	-21.8	-38.3	-25.7
	10	31/01		-33.0	5.3	-1.9	-25.4	-78.1	-54.5	-33.1	-4.7	-53.7	-21.0	-25.7	-38.3	-36.5
	10	07/02		-33.6	6.0	-7.9	-20.7	-69.3	-41.3	-28.1	-6.1	-51.1	-19.1	-24.4	-38.3	-21.6
M2B	10	09/02	*Injection*	-33.5	7.9	-15.6	-19.5	-68.5	-38.1	-28.5	-1.2	-40.9	-18.6	-26.4	-38.3	-35.1
	10	14/02		-23.6	4.8	-12.9	-12.3	-64.7	7.4	-29.7	3.1	-32.2	-8.6	-19.8	-38.3	-
	12.5	16/02		-19.8	7.0	-13.8	-11.1	-64.2	-29.5	-28.7	-5.2	-25.2	-9.9	-19.7	-38.3	-5.4
	12.5	20/02		-14.6	1.5	-5.7	-5.0	-63.3	-28.2	-27.7	11.7	-1.2	-0.5	-100.0	**31.3**	18.9
	12.5	23/02		-14.4	3.2	-3.9	-2.9	-62.4	-32.4	-28.3	6.9	0.2	-1.3	-7.8	-38.3	**33.8**
	12.5	28/02		-17.0	7.3	-8.5	-5.4	-61.0	-29.3	-30.6	4.2	-8.9	-1.7	-12.6	-38.3	14.9
	12.5	01/03		-20.7	4.5	-5.8	-6.2	-60.4	-28.9	-30.8	8.6	-15.4	-2.1	-14.0	-38.3	13.5
	0	05/03		-18.2	4.3	-7.3	-3.5	-58.1	-25.1	-31.0	12.5	-21.7	3.7	-12.8	-38.3	10.8
	0	08/03		-19.0	5.7	-5.7	-1.5	-57.3	-26.6	-29.2	11.5	-20.8	-0.5	-15.4	-38.3	-1.4
	0	12/03	*PI*	-15.9	5.8	-8.5	-5.6	-59.3	-28.9	-34.3	10.6	-23.8	-2.1	11.9	-38.3	5.4
	0	15/03		-22.6	4.9	-11.4	-5.6	-59.9	-24.9	-33.7	11.0	-23.7	-2.3	-15.0	-38.3	12.2
	0	17/07		-37.6	8.6	-18.3	-21.0	-78.6	-80.0	-36.7	-7.9	-77.6	-38.5	-	-38.3	-27.0

The parameters showing changes greater than 20% include EC, Ca, Mg, Fe, HCO_3^-, Ba, Sr, and Mn. Total alkalinity, although not listed in the table, should also be considered sensitive to CO_2 injection because of its direct relationship with HCO_3^-, a key chemical species. The observed behavior of most of these parameters (excluding Fe and Mn) aligns with the findings of Cahill et al. (2014), Do et al. (2022), Humez et al. (2014), Kharaka et al. (2010), Mickler et al. (2013), Peter et al. (2012), Pezard et al. (2016), Trautz et al. (2013) and Yang et al. (2013, 2014), supporting the conclusion that these hydrochemical variables are indeed sensitive to CO_2 injection, even at relatively low injection rates and under conditions of high interaction with recharge water (in this case, rainfall). This pattern, which is consistent with the pulse-like response of these chemical species described in the literature, suggests that ion exchange is the dominant geochemical mechanism driving this process.

This suggests that in the event of CO_2 leakage into a relatively deep monitored aquifer above the injection complex in a real industrial-scale CCS project, hydrochemical changes could still be monitored as indicators of leakage, even in the presence of an external water source (e.g., a leaky confined aquifer or proximity to a recharge zone), provided that the long-term natural baseline is well established. Notably, pH changes were not consistently identified as sensitive indicators of CO_2 leakage in this study. This can be

primarily attributed to the dilution effect of recharge water with pH values likely exceeding 6, which buffered the impact of CO_2 injection.

In contrast, the behavior of Fe and Mn across the referenced studies varies. While most studies report an increase in these elements due to CO_2 injection, some, such as Cahill et al. (2014), reported a decrease. In the present study, the levels of both elements increased, particularly during the later stages of CO_2 injection, indicating their sensitivity to this process. This response is likely due to desorption and/or dissolution from Al/Fe/Mn oxyhydroxides (Lee et al. 2016; Gupta and Yadav 2020), which are commonly altered minerals or amorphous phases resulting from weathering of granite. Given their sustained percentage variation above 20% during the CO_2 injection phase, the variables identified herein (EC, Ca, Mg, Fe, HCO_3^-, Ba, Sr, and Mn) appear to be the most reliable hydrochemical tracers for the detection of unintended CO_2 leakage in aquifers surrounding geological carbon storage sites, particularly within shallow monitoring networks.

4.4. Implications of δ^{13}C-DIC as a natural tracer

As highlighted by Clark & Fritz (2013), the distribution of DIC species is primarily controlled by pH, while fractionation between each aqueous species and CO_2 (g)—whether naturally present in the soil gas or, in this case, injected—also depends on temperature. Considering the samples from M1A and M1B collected during the period when δ^{13}C-DIC reached its minimum values (February 16, sampling campaign SI16), with measured δ^{13}C-DIC values of -29.1‰ and -25.7‰, respectively, and following the isotope fractionation and mass balance calculations detailed in the Supplementary Material (Eqs. 1–9), it can be estimated—only as indicative—that injected CO_2 accounted for approximately 71% (M1A) and 60% (M1B) of the δ^{13}C-DIC signal, assuming that the soil gas consisted solely of injected CO_2 during this period.

Notably, as hydrochemical parameters began to significantly change even before February 16, the data indicate that the contributions of injected CO_2 below 60% were sufficient to trigger the observed responses. Although δ^{13}C-DIC has certain limitations as a tracer for diagnosing unintended CO_2 leakage in CCS projects (e.g., depending on a clear isotopic contrast between injected CO_2 and background DIC), these findings support its reliability as a natural tracer in this context. These results are consistent with the conclusions of previous studies (Yang et al., 2013; Humez et al., 2014; Newell et al., 2014; Do et al., 2022).

4.5. Bivariate plots and geochemical processes

Groundwater chemistry data from all the wells were used to recognize geochemical processes and help identify the main mechanisms regulating the relationship with CO_2. In this case, rock weathering and dissolution processes were identified through commonly used bivariate plots (Figure 12). According to Gaillardet's plots (Gaillardet et al. 1999), the majority of the samples lie within the silicate weathering field, which is characterized by intermediate Ca/Na and HCO_3^-/Na ratios on a logarithmic graph (Figure 12a and b). Some samples have a greater tendency to approach the carbonate dissolution field and eventually fall within the designated area, but this is restricted to samples from well M4B or an outlier from M1A. A further approach to evaluate this process is by plotting the sum of Ca + Mg (meq/L) in relation to the total sum of cations (TC, in meq/L).

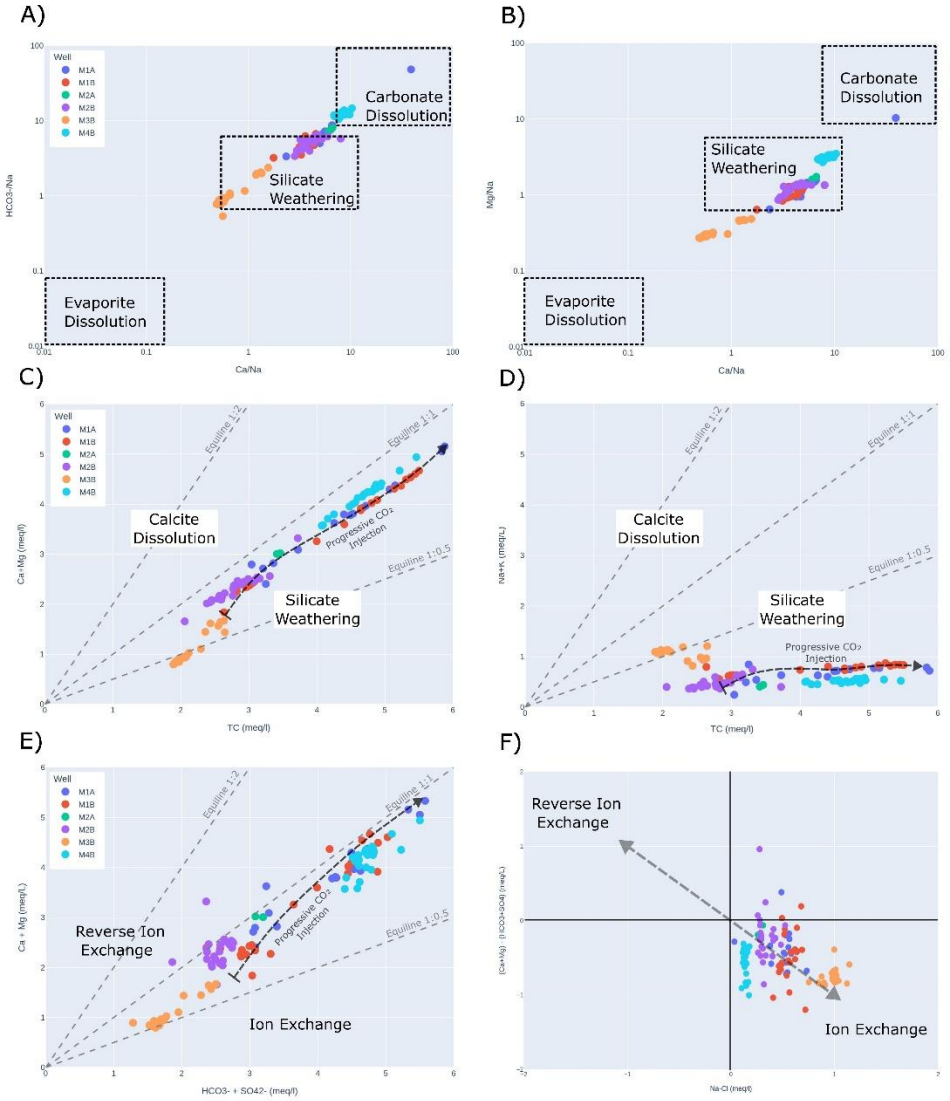


Fig 12 Bivariate geochemical plots: (a) and (b) depict Gaillardet's sodium-normalized HCO_3^- and Mg versus Ca/Na relationship; (c) and (d) show total cations (TC) versus Ca + Mg and Na + K (in meq/L); and (e) and (f) evaluate ion exchange processes with Ca + Mg versus HCO_3^- + SO_4^{2-} (in meq/L) and (Ca + Mg) – (HCO_3^- + SO_4^{2-}) versus Na - Cl (in meq/L), respectively

In this case, the dominance of Ca and Mg over Na and K is illustrated in the plots of TC versus Ca + Mg (Figure 12c) and TC versus Na + K (Figure 12d). The graphs reveal that the groundwater samples are positioned between the 1:0.5 equiline and slightly below the 1:1 equiline for Ca + Mg; the latter line indicates conditions consistent with calcite dissolution. Additionally, the plot of Na + K versus TC indicates that most samples lie below or near the 1:0.5 equiline. As CO_2 injection progresses, an increasing contribution of Ca + Mg is observed alongside a rise in TDS, although still below the carbonate dissolution line, while the sum of Na + K remains relatively unchanged as the CO_2–water–mineral interactions advance. These relationships suggest that silicate weathering contributes to the presence of these ions in groundwater (Stallard and Edmond 1983; Senthilkumar and Elango 2013; Kanagaraj and Elango 2019; Nethononda et al. 2019).

Nonetheless, as previously discussed, significant increases in Ca, Mg, Ba, and Sr—elements commonly associated with carbonate dissolution—have been observed. To elucidate the geochemical processes that

may explain this mechanism, a plot of Ca + Mg versus $HCO_3^- + SO_4^{2-}$ is used to assess the occurrence of ion exchange processes (Figure 12e and f). As shown in Figure 12e, most samples are plotted below the 1:1 equiline, indicating a direct ion exchange process (Brindha et al. 2020; Mthembu et al. 2020; Refat Nasher and Humayan Ahmed 2021). Typically, during ion exchange, Ca^{2+} cations are retained in the soil, while Na^+ cations are released into groundwater. Conversely, in reverse ion exchange, Na^+ cations are retained in the soil, while Ca^{2+} cations are released into groundwater. In our case, as CO_2 injection progresses, samples from wells M1A and M1B tend to approach and sometimes exceed the 1:1 equiline, entering the reverse ion exchange field. This behavior suggests that as CO_2 interacts with the mineral matrix, divalent cations are preferentially released from the aquifer material, leading to an increased presence in the groundwater.

This process has been attributed to the pulse-like behavior of Ca, Mg, Na, K, Sr, Ba, and HCO_3^- in various studies in aquifers dominated by silicate minerals (Peter et al. 2012; Trautz et al. 2013; Cahill et al. 2014), including Do et al. (2022), which corroborate our findings. Furthermore, although no carbonate minerals have been identified in our study area, the possible origin of carbonate minerals and associated elements could be related to the historical application of lime for soil pH correction. Although the study area has not been used for agricultural practices in the past 10 years, Ca and other elements may still be adsorbed in clay minerals, as documented by Cherian et al. (2018). These minerals are commonly found across all the hydrostratigraphic units of the profile, particularly in the zones where groundwater samples were collected.

Iron and manganese concentrations can be significantly influenced by redox conditions and desorption processes, especially under increasing acidity (Appelo and Postma 2005; Berkowitz et al. 2014). Iron, in its ferric form (Fe^{3+}), is generally insoluble under oxidizing conditions, whereas it becomes soluble as ferrous iron (Fe^{2+}) under reducing conditions. In this study, ORP measurements indicated a progressive increase in its values for almost all wells (except M4B) throughout the CO_2 injection phase, which approached more oxidizing conditions. ORP values eventually surpassed 0 mV only during the immediate postinjection period and at SP25 (Figure 4). Concurrently, during this latter phase, Fe concentrations began to decrease, which can be attributed to the precipitation of Fe^{3+} as Fe-oxyhydroxides (Drever 1997). However, the increase in Fe levels during the CO_2 injection phase under mildly acidic conditions may suggest an intermediate reaction pathway involving the desorption of Fe^{2+} from exchange and surface sorption sites, as previously discussed by Appelo et al., (1999) and Appelo and Postma (2005).

4.6. Influence of precipitation events

The impact of precipitation on the CO_2(g) concentration and CO_2(g) flux in the soil has been previously examined by Delsarte et al. (2021) under conditions very similar to those in this study. They reported that artificial rainfall events led to a decrease of more than 450% in CO_2 concentration levels (with concentrations decreasing from 388 to 65 g/m³). The upward CO_2(g) fluxes also decreased significantly, from approximately 40–35 mg/m²/min to less than 10 mg/m²/min, and in some cases, even below 1 mg/m²/min.

Furthermore, although rainwater samples were not collected onsite, Migliavacca et al. (2005) conducted an extensive study of bulk atmospheric precipitation over the hydrographic basin that encompasses the study area, spanning an entire year (January–December 2002). For comparison, the average (n=107) bulk

669 precipitation composition revealed the following values: pH 6.13, EC 13.2 µS/cm, HCO_3^- 1.4 mg/L, Cl^-
670 0.66 mg/L, SO_4^{2-} 1.45 mg/L, Ca 0.66 mg/L, Mg 0.16 mg/L, Na 0.44 mg/L, and K 0.33 mg/L, indicating
671 very dilute water compared to the groundwater analyzed in this study.
672 During our experiment, from January 8 to March 15, approximately 300 mm of accumulated
673 precipitation was recorded. Between March 15 and July 17, a remarkable 1,100.04 mm of rainfall was
674 recorded. It is one of the most significant sequences of precipitation events ever observed in southern Brazil
675 (Clarke et al. 2024). Throughout the CO_2 injection phase, the daily precipitation often exceeded 30 mm and
676 occasionally surpassed 50 mm, as shown in the previous graphs. Thus, it is reasonable to conclude that the
677 observed reduction in concentration increases and significant decreases in certain chemical species were
678 likely due to the dilution effects of rainwater and the attenuation of dissolved CO_2(g). This dilution likely
679 resulted in a diminished overall impact compared with the findings reported in other studies, such as those
680 summarized in Gupta and Yadav (2020), Lee et al. (2016), Roberts and Stalker (2020), Zheng et al. (2021)
681 and Zielinski et al. (2023). However, fluctuations in water levels may also affect redox processes,
682 contributing to the observed changes and explaining variations in parameters such as Fe and Mn.

683 **5. Conclusions**

684 In this study, we observed consistent spatiotemporal variations in physicochemical parameters, major
685 ions, trace elements, and δ^{13}C-DIC during a controlled CO_2 release experiment in a silicate-rich, multilayer
686 shallow aquifer. These variations were linked to the arrival of the CO_2-impacted groundwater plume at
687 monitoring wells located in close geographic proximity. CO_2 injection was conducted at three different
688 rates (5, 10, and 12.5 kg/day). The results demonstrated that higher release rates enhanced the clarity of
689 hydrochemical parameter detection, making it easier to observe changes in groundwater chemistry.
690 However, given the site's shallow nature, precipitation events were also observed to influence the
691 magnitude of the hydrogeochemical changes, and the results sometimes differed from the findings of other
692 referenced studies.
693 The breakthrough point of the CO_2-impacted groundwater plume was distinctly identified in wells M1A
694 and M1B by increases in EC, total alkalinity (and consequently HCO_3^-), PCO_2, and a range of elements and
695 chemical compounds, including Ca, Mg, K, Sr, Ba, Na, Fe, Si, Cl^- and δ^{13}C-DIC. These changes became
696 particularly pronounced when the CO_2 injection rate was increased to 10 kg/day. PCA and correlation
697 analyses were instrumental in identifying groups of CO_2-impacted wells and tracking the evolution of
698 dissolved ions in relation to PCO_2. PCA revealed that wells M3B, M4B, and M2B were either unaffected
699 or only weakly impacted by CO_2. These analyses also reduced dimensionality by focusing on variables that
700 exhibited a strong direct correlation with the proxy PCO_2, including EC, pH, HCO_3^-, Cl^-, total alkalinity,
701 Ca, Mg, Na, Si, Ba, Sr, Fe, Mn and δ^{13}C-DIC. Subsequent comparison of these variables with the calculated
702 PCO_2 for each well enabled the establishment of a chronological evolutionary trend. This analysis indicated
703 that certain variables exhibited clearer patterns during background conditions (BG) and low injection rates,
704 with more pronounced changes occurring at an injection rate of 10 kg/day and peak changes occurring at
705 an injection rate of 12.5 kg/day. Particularly noteworthy was the effectiveness of δ^{13}C-DIC as a natural
706 tracer, which demonstrated clear advantages for detecting and interpreting the influence of injected CO_2 in
707 this study.

Bivariate geochemical plots indicate that the majority of samples are plotted within the silicate weathering field. However, a more detailed comparison with other studies and an analysis of element behavior suggest that the dominant geochemical mechanism responsible for the release of Ca, Mg, Na, K, Sr, Ba, and HCO_3^- is direct or reverse ion exchange. In contrast, the behavior of Fe and Mn suggests an intermediate reaction pathway involving the desorption of Fe^{2+} from exchange and surface sorption sites.

Although precipitation events clearly influence CO_2(g) flux and mixing with CO_2-impacted groundwater alters the magnitude of physicochemical and chemical parameters, the sensitivity to CO_2 leakage can be assessed against the lower and upper control limits of each variable. In this context, a variation exceeding 20% indicates that EC, Ca, Mg, Fe, HCO_3^-, Ba, Sr, Mn and δ^{13}C-DIC can be confidently used as indicators of leakage. Notably, the observed behavior of Fe and Mn warrants special attention, as their concentrations exceed the maximum contaminant levels prescribed by national and international regulations. This is particularly concerning given that similar behavior has been reported in long-term, naturally CO_2-impacted groundwater in silicate bedrock formations (granite and gneiss) with limited buffering capacity.

Statements and declarations

Funding

This work was funded through the RD&I project ECO2A, with financial support from the *Financiadora de Estudos e Projetos (FINEP)*, an agency affiliated with the Brazilian Ministry of Science, Technology and Innovation (MCTI), under Reference No. 0132/21.

Competing interests

The authors have no relevant financial or non-financial interests to disclose.

Author contributions

All authors contributed to the study conception and design. Material preparation, data collection, and analysis were conducted by João Pedro T. Zielinski, William Jeovanini Fucks, Mauren Espinosa Gaspar, and Fernando Hamerski. João Pedro T. Zielinski drafted the manuscript, and all authors reviewed, revised, and approved the final version.

References

ABNT (2010) Amostragem de água subterrânea em poços de monitoramento — Métodos de purga. NBR 15847, pp 1–15

Appelo CAJ, Drijver B, Hekkenberg R, de Jonge M (1999) Modeling in situ iron removal from ground water. Groundwater 37:811–817. https://doi.org/10.1111/j.1745-6584.1999.tb01179.x

Appelo CAJ, Postma D (2005) Geochemistry, groundwater and pollution. Elsevier, Amsterdam. https://doi.org/10.1016/0016-7037(94)90585-1

Assayag N, Matter J, Ader M et al (2009) Water–rock interactions during a CO2 injection field-test: implications on host rock dissolution and alteration effects. Chem Geol 265:227–235. https://doi.org/10.1016/j.chemgeo.2009.02.007

744 ASTM (2018) Standard guide for purging methods for wells used for ground water quality
745 investigations. D6452-18, pp 1–6

746 ASTM (2019) Standard guide for sampling ground-water monitoring wells. D4448-01(2019), pp 1–
747 17

748 Azar C, Lindgren K, Larson E, Möllersten K (2006) Carbon capture and storage from fossil fuels and
749 biomass – costs and potential role in stabilizing the atmosphere. Clim Change 74:47–79.
750 https://doi.org/10.1007/s10584-005-3484-7

751 Beaubien SE, Ruggiero L, Annunziatellis A et al (2015) The importance of baseline surveys of near-
752 surface gas geochemistry for CCS monitoring, as shown from onshore case studies in northern and
753 southern Europe. Oil Gas Sci Technol Rev IFP Energies Nouv 70:615–633.
754 https://doi.org/10.2516/ogst/2014009

755 Benson SM, Cole DR (2008) CO2 sequestration in deep sedimentary formations. Elements 4:325–
756 331. https://doi.org/10.2113/gselements.4.5.325

757 Benson SM, Hepple R, Apps J et al (2002) Lessons learned from natural and industrial analogues for
758 storage of carbon dioxide in deep geological formations. Berkeley, CA

759 Berkowitz B, Dror I, Yaron B (2014) Contaminant geochemistry: interactions and transport in the
760 subsurface environment. Springer, Berlin Heidelberg

761 Brindha K, Paul R, Walter J et al (2020) Trace metals contamination in groundwater and implications
762 on human health: comprehensive assessment using hydrogeochemical and geostatistical methods.
763 Environ Geochem Health 42:3819–3839. https://doi.org/10.1007/s10653-020-00637-9

764 Cahill AG, Marker P, Jakobsen R (2014) Hydrogeochemical and mineralogical effects of sustained
765 CO2 contamination in a shallow sandy aquifer: a field-scale controlled release experiment. Water
766 Resour Res 53:5375–5377. https://doi.org/10.1002/2013WR014294

767 Cahill AG, Jakobsen R (2015) Geochemical modeling of a sustained shallow aquifer CO2 leakage
768 field study and implications for leakage and site monitoring. Int J Greenh Gas Control 37:127–141.
769 https://doi.org/10.1016/j.ijggc.2015.03.011

770 Cherian C, Kollannur NJ, Bandipally S, Arnepalli DN (2018) Calcium adsorption on clays: effects
771 of mineralogy, pore fluid chemistry and temperature. Appl Clay Sci 160:282–289.
772 https://doi.org/10.1016/j.clay.2018.02.034

773 Choi H, Piao J, Woo NC, Cho H (2017) Hydrochemical variations in selected geothermal
774 groundwater and carbonated springs in Korea: a baseline study for early detection of CO2 leakage.
775 Environ Geochem Health 39:109–123. https://doi.org/10.1007/s10653-016-9813-5

776 Clark ID, Fritz P (2013) Environmental isotopes in hydrogeology. CRC Press, Boca Raton

777 Clarke B, Barnes C, Rodrigues R et al (2024) Climate change, El Niño and infrastructure failures
778 behind massive floods in southern Brazil. London

779 Conover WJ (1999) Practical nonparametric statistics, 3rd edn. John Wiley & Sons, New York

780 Coplen TB, Brand WA, Gehre M et al (2006) New guidelines for δ13C measurements. Anal Chem
781 78:2439–2441. https://doi.org/10.1021/ac052027c

782 Cuéllar-Franca RM, Azapagic A (2015) Carbon capture, storage and utilisation technologies: a
783 critical analysis and comparison of their life cycle environmental impacts. J CO2 Util 9:82–102.
784 https://doi.org/10.1016/j.jcou.2014.12.001

785 Delsarte I, Cohen GJV, Momtbrun M et al (2021) Soil carbon dioxide fluxes to atmosphere: the role
786 of rainfall to control CO2 transport. Appl Geochem 127:104854.
787 https://doi.org/10.1016/j.apgeochem.2020.104854

788 Do H-K, Yu S, Ryuh YG et al (2022) Tracing CO2 leakage and migration using the
789 hydrogeochemical tracers during a controlled CO2 release field test. Appl Geochem 143:105390.
790 https://doi.org/10.1016/j.apgeochem.2022.105390

791 Do H-K, Yun S-T, Yu S et al (2020) Evaluation of long-term impacts of CO2 leakage on groundwater
792 quality using hydrochemical data from a natural analogue site in South Korea. Water 12:1457.
793 https://doi.org/10.3390/w12051457

794 Drever JI (1997) The geochemistry of natural waters: surface and groundwater environments.
795 Prentice Hall, Upper Saddle River

796 Freeze RA, Cherry JA (1979) Groundwater. Prentice-Hall, Englewood Cliffs

797 Friedman I, O'Neil J, Cebula G (1982) Two new carbonate stable-isotope standards. Geostand
798 Geoanal Res 6:11–12. https://doi.org/10.1111/j.1751-908X.1982.tb00340.x

799 Gaillardet J, Dupré B, Louvat P, Allègre CJ (1999) Global silicate weathering and CO2 consumption
800 rates deduced from the chemistry of large rivers. Chem Geol 159:3–30.
801 https://doi.org/10.1016/S0009-2541(99)00031-5

802 Gupta PK, Yadav B (2020) Leakage of CO2 from geological storage and its impacts on fresh soil–
803 water systems: a review. Environ Sci Pollut Res 27:12995–13018. https://doi.org/10.1007/s11356-
804 020-08203-7

805 Humez P, Lions J, Négrel P, Lagneau V (2014a) CO2 intrusion in freshwater aquifers: review of
806 geochemical tracers and monitoring tools, classical uses and innovative approaches. Appl Geochem
807 46:95–108. https://doi.org/10.1016/j.apgeochem.2014.02.008

808 Humez P, Négrel P, Lagneau V et al (2014b) CO2-water-mineral reactions during CO2 leakage:
809 geochemical and isotopic monitoring of a CO2 injection field test. Chem Geol 368:11–30.
810 https://doi.org/10.1016/j.chemgeo.2014.01.001

811 Iglesias RS, Romio C, Melo CL et al (2019) Modeling CO2 flow in support of a shallow subsurface
812 controlled leakage field test. Greenh Gases Sci Technol 9:1027–1042.
813 https://doi.org/10.1002/ghg.1917

814 IPCC (2005) Special report on carbon dioxide capture and storage. New York, NY, USA

815 Jolliffe IT (1986) Principal component analysis. Springer, New York, NY

816 Kanagaraj G, Elango L (2019) Chromium and fluoride contamination in groundwater around leather
817 tanning industries in southern India: implications from stable isotopic ratio δ53Cr/δ52Cr,
818 geochemical and geostatistical modelling. Chemosphere 220:943–953.
819 https://doi.org/10.1016/j.chemosphere.2018.12.105

820 Kharaka YK, Thordsen JJ, Kakouros E et al (2010) Changes in the chemistry of shallow groundwater
821 related to the 2008 injection of CO2 at the ZERT field site, Bozeman, Montana. Environ Earth Sci
822 60:273–284. https://doi.org/10.1007/s12665-009-0401-1

823 Lasaga AC (1984) Chemical kinetics of water-rock. J Geophys Res 89:4009–4025

824 Lawter A, Qafoku NP, Wang G et al (2016) Evaluating impacts of CO2 intrusion into an
825 unconsolidated aquifer: I. Experimental data. Int J Greenh Gas Control 44:323–333.
826 https://doi.org/10.1016/j.ijggc.2015.07.009

827 Lee KK, Lee SH, Yun ST, Jeen SW (2016) Shallow groundwater system monitoring on controlled
828 CO2 release sites: a review on field experimental methods and efforts for CO2 leakage detection.
829 Geosci J 20:569–583. https://doi.org/10.1007/s12303-015-0060-z

830 Lions J, Devau N, de Lary L et al (2014) Potential impacts of leakage from CO2 geological storage
831 on geochemical processes controlling fresh groundwater quality: a review. Int J Greenh Gas Control
832 22:165–175. https://doi.org/10.1016/j.ijggc.2013.12.019

Ma J, Zhou Y, Zheng Y et al (2024) Advances in geochemical monitoring technologies for CO2 geological storage. Sustainability 16:6784. https://doi.org/10.3390/su16166784

Melo CL, De Moreira AC, Goudinho FS et al (2017) CO2MOVE Project: the new Brazilian field lab fully dedicated to CO2 MMV experiments. Energy Procedia, pp 3699–3715

Mickler PJ, Yang C, Scanlon BR et al (2013) Potential impacts of CO2 leakage on groundwater chemistry from laboratory batch experiments and field push-pull tests. Environ Sci Technol 47:10694–10702. https://doi.org/10.1021/es401455j

Migliavacca D, Teixeira E, Wiegand F et al (2005) Atmospheric precipitation and chemical composition of an urban site, Guaíba hydrographic basin, Brazil. Atmos Environ 39:1829–1844. https://doi.org/10.1016/j.atmosenv.2004.12.005

Mthembu PP, Elumalai V, Brindha K, Li P (2020) Hydrogeochemical processes and trace metal contamination in groundwater: impact on human health in the Maputaland Coastal Aquifer, South Africa. Expo Health 12:403–426. https://doi.org/10.1007/s12403-020-00369-2

Nethononda VG, Elumalai V, Rajmohan N (2019) Irrigation return flow induced mineral weathering and ion exchange reactions in the aquifer, Luvuvhu catchment, South Africa. J Afr Earth Sci 149:517–528. https://doi.org/10.1016/j.jafrearsci.2018.09.001

Newell DL, Larson TE, Perkins G et al (2014) Tracing CO2 leakage into groundwater using carbon and strontium isotopes during a controlled CO2 release field test. Int J Greenh Gas Control 29:200–208. https://doi.org/10.1016/j.ijggc.2014.08.015

Oelkers EH, Cole DR (2008) Carbon dioxide sequestration: a solution to a global problem. Elements 4:305–310. https://doi.org/10.2113/gselements.4.5.305

Parkhurst DL, Appelo CAJ (2013) Description of input and examples for PHREEQC version 3—A computer program for speciation, batch-reaction, one-dimensional transport, and inverse geochemical calculations. US Geological Survey Techniques and Methods

Peter A, Lamert H, Beyer M et al (2012) Investigation of the geochemical impact of CO2 on shallow groundwater: design and implementation of a CO2 injection test in Northeast Germany. Environ Earth Sci 67:335–349. https://doi.org/10.1007/s12665-012-1700-5

Pezard PA, Denchik N, Lofi J et al (2016) Time-lapse downhole electrical resistivity monitoring of subsurface CO2 storage at the Maguelone shallow experimental site (Languedoc, France). Int J Greenh Gas Control 48:142–154. https://doi.org/10.1016/j.ijggc.2015.12.005

Qafoku NP, Lawter AR, Bacon DH et al (2017) Review of the impacts of leaking CO2 gas and brine on groundwater quality. Earth Sci Rev 169:69–84. https://doi.org/10.1016/j.earscirev.2017.04.010

Refat Nasher NM, Humayan Ahmed Md (2021) Groundwater geochemistry and hydrogeochemical processes in the Lower Ganges-Brahmaputra-Meghna River Basin areas, Bangladesh. J Asian Earth Sci X 6:100062. https://doi.org/10.1016/j.jaesx.2021.100062

Roberts JJ, Stalker L (2020) What have we learnt about CO2 leakage from CO2 release field experiments, and what are the gaps for the future? Earth Sci Rev 209:102939. https://doi.org/10.1016/j.earscirev.2019.102939

Schulz A, Vogt C, Lamert H et al (2012) Monitoring of a simulated CO2 leakage in a shallow aquifer using stable carbon isotopes. Environ Sci Technol 46:11243–11250. https://doi.org/10.1021/es3026837

Senthilkumar M, Elango L (2013) Geochemical processes controlling the groundwater quality in lower Palar river basin, southern India. J Earth Syst Sci 122:419–432. https://doi.org/10.1007/s12040-013-0284-0

Shapiro SS, Wilk MB (1965) An analysis of variance test for normality (complete samples). Biometrika 52:591–611. https://doi.org/10.1093/biomet/52.3-4.591

Stallard RF, Edmond JM (1983) Geochemistry of the Amazon: 2. The influence of geology and weathering environment on the dissolved load. J Geophys Res Oceans 88:9671–9688. https://doi.org/10.1029/JC088iC14p09671

Stumm W, Morgan JJ (1996) Aquatic chemistry, chemical equilibria and rates in natural waters, 3rd edn. John Wiley & Sons, Inc., New York

Trautz RC, Pugh JD, Varadharajan C et al (2013) Effect of dissolved CO2 on a shallow groundwater system: a controlled release field experiment. Environ Sci Technol 47:298–305. https://doi.org/10.1021/es301280t

Utley RE, Martin-Roberts E, Utting N et al (2023) Multi-isotope geochemical baseline study of the Carbon Management Canada Research Institutes CCS Field Research Station (Alberta, Canada), prior to CO2 injection. Earth Sci Syst Soc 3:10069. https://doi.org/10.3389/esss.2023.10069

Wang G, Qafoku NP, Lawter AR et al (2016) Geochemical impacts of leaking CO2 from subsurface storage reservoirs to an unconfined oxidizing carbonate aquifer. Int J Greenh Gas Control 44:310–322. https://doi.org/10.1016/j.ijggc.2015.07.002

Wang J, Xiong W, Gardiner JB et al (2023) A geochemically informed leak detection (GILD) model for CO2 injection sites. Appl Geochem 155:105691. https://doi.org/10.1016/j.apgeochem.2023.105691

Supplementary Files

This is a list of supplementary files associated with this preprint. Click to download.

- PaperEESZielinskietal2026Supplementarymaterials.docx